

Cite this: *Digital Discovery*, 2023, 2, 1506

# Active learning for efficient navigation of multi-component gas adsorption landscapes in a MOF†

Krishnendu Mukherjee,  Etinosa Osaro  and Yamil J. Colón \*

In recent decades, metal–organic frameworks (MOFs) have gained recognition for their potential in multicomponent gas separations. Though molecular simulations have revealed structure–property relationships of MOF–adsorbate systems, they can be computationally expensive and there is a need for surrogate models that can predict the adsorption data faster. In this work, an active learning (AL) protocol is introduced that can predict multicomponent gas adsorption in a MOF for a range of thermodynamic conditions. This methodology is applied to build a model for the adsorption of three different gas mixtures (CO<sub>2</sub>–CH<sub>4</sub>, Xe–Kr, and H<sub>2</sub>S–CO<sub>2</sub>) in the MOF Cu–BTC. A Gaussian process regression (GPR) model is used to fit the data as well to leverage its predicted uncertainty to drive the learning. The training data is generated using grand-canonical Monte Carlo (GCMC) simulations as points are iteratively added to the model to minimize the predicted uncertainty. Also, a criteria which captures the perceived performance of the GPs is introduced to terminate the AL process when the perceived accuracy threshold is met. The three systems are tested for a pressure–mole fraction ( $P$ – $X$ ), and a pressure–mole fraction–temperature ( $P$ – $X$ – $T$ ) feature space. It is demonstrated that AL one only needs a fraction of the data from simulations to build a reliable surrogate model for predicting mixture adsorption. Further, the final GP fit from AL outperforms ideal adsorbed solution theory predictions.

Received 6th June 2023  
Accepted 23rd August 2023

DOI: 10.1039/d3dd00106g

rsc.li/digitaldiscovery

## 1 Introduction

Metal–organic frameworks (MOFs), a class of crystalline nanoporous materials, are known for their high surface area and pore volume.<sup>1</sup> These materials are self-assembled from two components – organic linker molecules and inorganic metal nodes or metal clusters – a property that provides infinite choices of structures that can be synthesized in a laboratory. MOFs have demonstrated applicability for energy storage, gas separations, and sensing.<sup>2–7</sup> Despite the potential of these materials and their increasing numbers reported in experiments, there is a challenge to determine which are the best MOFs and what are the conditions (*e.g.*, temperature, pressure) that maximize their performance. For these decisions, the adsorption isotherms are very useful. This data helps to select structures that might be a good fit depending on either selectivity, or adsorption (say at condition of pressure and temperature of  $P$  and  $T$ , respectively) or just total gas uptake at a  $T$  but for different pressures.<sup>8</sup> Molecular simulations have played an important role in the design and discovery of MOFs for a variety of applications.<sup>9</sup> However, the number of MOFs in existence has kept increasing and new procedures have been introduced to enhance computational capabilities.<sup>10–13</sup> The use of large-scale,

high-throughput computational screening techniques on databases of MOF structures (experimental or computationally generated) has revealed structure–property relationships and identified top performing materials for many applications.<sup>14–19</sup>

In this work, we focus on multi-component adsorption in MOFs. Gas mixtures are ubiquitous in nature and studying their interactions with materials is essential for a number of purposes. For example, MOFs can be used for separating impurities in hydrogen gas which then can be fed to hydro-cracker and hydro-processing units, to capture carbon dioxide for tackling climate change, or for separating hydrogen sulphide from refinery waste streams to eventually extract solid sulphur as well as enhance gasoline quality.<sup>20–22</sup> In many of these applications, nanoporous materials can be utilized for adsorption and separation of different species in gas mixtures. Since multicomponent gas adsorption can take place at a variety of conditions, it is important to understand how they affect MOF adsorption for the relevant set of adsorbates in the mixture. Conventionally, grand-canonical Monte Carlo (GCMC) simulations are employed for generating adsorption isotherm for these mixtures in MOFs, and depending on the system size they can take considerable time to finish.<sup>23,24</sup> Further, each GCMC simulation is done at specific operating conditions and to get an isotherm one has to conduct many such simulations. This can rapidly increase the total computational cost of a project. Further, in many computing environments, the resources might be very limited. For example, to calculate the

University of Notre Dame, Notre Dame, IN, USA. E-mail: ycolon@nd.edu

† Electronic supplementary information (ESI) available. See DOI: <https://doi.org/10.1039/d3dd00106g>

uptake for a  $n$  pressure  $\times$   $n$  temperature points, one has to conduct  $n^2$  number of simulations. Adding more features can very well prohibit the study and one has to either look for theoretical models or drastically reduce the design space. Thus, there is a need for a surrogate model which can provide us these properties with only a fraction of these conventional simulations/experiments from the input space.

### 1.1 Machine learning combined with molecular simulations for gas adsorption in MOFs

The emergence of big data has also allowed researchers to employ machine learning (ML) algorithms for a variety of chemistry applications.<sup>25,26</sup> Many of these ML models have been applied for gas adsorption and separation problems.<sup>27–35</sup> These models have provided important physical insight through the development of new descriptors capable of capturing important factors for applications of interest.<sup>36–40</sup> Further, alternate training methods such as transfer learning have also shown promise in terms of saving training cost while building these models.<sup>41,42</sup> However, therein lies a challenge and bottleneck for workflows that rely on ML for predictions—large dataset are needed for the proper training and deployment of many ML algorithms. In cases where obtaining high-fidelity data is difficult or prohibitive, the potential of ML algorithms and workflows is limited. Another concern with the way ML models are built, is the static nature of the training dataset. Conventionally, building the ML model using molecular simulation data is a passive learning strategy, in which all the training points are sampled at once by the user.<sup>9,26,43</sup> Hence, not all data contribute to the performance of the model equally. However, one can potentially get the same performance with far less number of training points if an intelligent and efficient way of choosing them is adopted. This would result in savings of computational power and efficient generation of training data. In the latter case, each new point added in the training set will contribute to a performance or betterment of the model. As pointed out earlier for adsorption problems, each simulation can be very expensive and particularly for multi-feature design space, it can quickly become very difficult to generate the desired training set. Hence, there is a need for surrogate model for multi-feature adsorption problems that are data efficient and that can generate the desired adsorption data with good performance.

### 1.2 Active learning as an alternate strategy for surrogate models

To tackle the challenges highlighted in building a ML-based model for mixture adsorption, an alternative strategy known as an active learning (AL) can be adopted.<sup>44</sup> In AL, the algorithm learns the desired target distribution in a ‘Bayesian’ style process, *i.e.* algorithm-directed new points are added to the training set and fitting is done iteratively until a certain criteria for learning is satisfied.<sup>43,45</sup> An AL methodology can balance the performance of the predictive models while minimizing the number of data points one is needed to acquire. This can be particularly attractive in situations where the feature space is “small” (such as composition of multicomponent adsorption

while varying temperature and pressure conditions) and/or time-consuming or resource-intensive experiments/simulations are needed. In this regard, GPRs (Gaussian process regression) stand out among other ML models. GPRs are flexible non-parametric models than can emulate any distribution with fewer data points. Further they provide an estimate of the standard deviation along with output, which is very useful to perform AL. Currently, there are two approaches in general adopted to model mixture adsorption. The first, which is also done in experiments, is to gather the pure component isotherms (many pressures, one temperature) and use them as inputs to ideal adsorbed solution theory (IAST) to make the predictions of the mixture adsorption at the chosen temperature.<sup>46</sup> This has many drawbacks, including the inaccuracies of IAST in many regions of the adsorption space and the necessity of the pure component isotherms.<sup>47</sup> The second, which is only for simulations as experiments of mixture adsorption are very rare, is to directly simulate the mixture adsorption with GCMC. This can be extremely data intensive as this is typically done by exhaustively simulating temperature, pressure, and compositions of the mixture. Given the intelligent selection of the simulations with the proposed AL approach, we can generate accurate surrogate models for the mixture with significant data savings. Further, for predicting isotherms, ML models have been used but very rarely have been employed in an active learning-oriented approach.<sup>48–50</sup> Furthermore, GPs have shown better performance for small sized datasets compared with models like Bayesian neural networks (BNNs) or neural network ensembles, which can also provide uncertainty estimates.<sup>51,52</sup> This makes GPs well suited for predictions for adsorption like problems where generating large dataset is expensive. These approaches are already gaining popularity in the molecular simulation space. For example, they have been used to calculate inter-molecular potential energy surfaces, force fields, and to connect different length and time scales.<sup>53–55</sup> Most of these works have used AL where the next simulation points were chosen based on predicted model uncertainty through a query-by-committee approach. In our previous work, we showed that AL can be used to predict adsorption isotherms for pure components in a MOF up to two features: temperature and pressure.<sup>56</sup> Recently, Osaro *et al.* also predicted pure-component isotherms of four different molecules using an AL approach and extended to multiple MOFs.<sup>57</sup> A branches and team also showed that phase diagram of deep-eutectics and ternary mixtures can be constructed efficiently using a thermodynamics-informed AL approach.<sup>58</sup> All these works have shown surrogate models built through AL require an order of magnitude less number of simulations. In this work, we apply the AL protocol to model adsorption of three binary gas mixtures (CO<sub>2</sub>–CH<sub>4</sub>, Xe–Kr, and H<sub>2</sub>S–CO<sub>2</sub>) in a MOF. These mixtures are selected due to the diverse characteristics of the individual components. CH<sub>4</sub> is non-polar with no charge while CO<sub>2</sub> is also non-polar but is charged. Xe and Kr are both noble gases, while H<sub>2</sub>S is charged as well as polar. The selection of these mixtures allows to explore a wide range of target adsorption distribution. For modeling the mixture adsorption, a dual-GPR (Gaussian process regression) model is applied for the mixtures using the



predicted uncertainty to select the next point.<sup>59</sup> A dual-GPR model here describes the application of two GPs, where each GP is a surrogate model tasked with learning the adsorption of only one species in the mixture. Therefore, the input features to both the GPs are same except for the mole-fraction (which is  $X_i$  to the first GP and  $1 - X_i$  to other GP), however both the GPs are trained to predict the uptake of their respective species in the mixture. Further, we introduce a new GP's perceived performance based convergence criteria called perceived accuracy to terminate the learning. We also test this protocol up to 3 features (pressure, mole fraction, and temperature). Finally, we demonstrate how the method can emulate adsorption isotherm for mixtures with only simulating a fraction of data points with reliable performance across different performance indicators. We compare the final GP results with ideal adsorbed solution theory (IAST)-predicted isotherms based on the Langmuir model.<sup>46,60</sup> Through this comparison we show that AL-generated adsorption isotherm outperforms IAST and are very close to the GCMC results for all three gas mixtures.

## 2 Methods

### 2.1 Ground truth generation

The Monte Carlo modeling suite, RASPA, was used to generate the ground truth.<sup>61</sup> Grand canonical Monte Carlo (GCMC) simulations were performed, which has resulted in accurate predictions when compared to experimental adsorption isotherms.<sup>23,24</sup> 5000 and 50 000 cycles were used for initialization and production respectively for generating the ground truth for the mixtures in the  $P$ - $X$  and  $P$ - $X$ - $T$  feature spaces. The ground truth data was used for two purposes. First, a part of the ground truth was used for providing the initial training set to the GP as well as to provide the next samples to the GP. Second, it was used as a benchmark to compare with the final GP fit (the state when AL ends), calculate the mean relative error (MRE), and correlation coefficient ( $R^2$ ) of the GP predicted adsorption with the GCMC simulations. The universal forcefield (UFF) was used for modeling the non-bonded interactions for Cu-BTC MOF and the Transferable Potentials for Phase Equilibria (TraPPE) for adsorbate molecules.<sup>62,63</sup> Charges for Cu-BTC were taken from Castillo *et al.*, where the Cu-BTC partial charges were obtained *via* fitting different set of charges to reproduce water adsorption data.<sup>64,65</sup> Furthermore, the combination of GCMC simulated isotherm based on UFF forcefield and TraPPE for mixture adsorbates have been previously utilized for mixtures simulation. Zhong and team performed GCMC simulations for equimolar binary mixtures of  $\text{CO}_2$ ,  $\text{CH}_4$ , and  $\text{H}_2$  in Cu-BTC MOF and found very close agreement with experiments.<sup>66</sup> Wang and coworkers also studied many hydrocarbon mixtures with carbon dioxide using TraPPE models in Cu-BTC and found excellent matching with experimental data.<sup>67</sup> Also, the IAST adsorption data was produced from fitting pure-component isotherm of the relevant gases in the mixtures using py-IAST developed by Simon and coauthors.<sup>46,68</sup> The Langmuir model with model isotherm() function of py-IAST was used to generate the IAST prediction from the pure component isotherms of the respective species. The pure component isotherm were based on the same pressure and

temperature conditions for which IAST prediction for the mixture condition were generated.

### 2.2 Initial training set selection criteria

The initial training set selection for this work was based on 'boundary-informed' scheme, as first detailed in our previous work.<sup>56</sup> This scheme is based on adding the pressure grid points in a geometric progression with a factor of 10. Thus, it covers both the low- and high-pressure points within the boundaries of the test dataset. The rest of the features in the scheme are linearly distributed within the defined limits. The points for the pressure feature were set at the boundaries of range (such as  $10^{-6}$ ,  $10^{-5}$ ,  $10^{-4}$ , and so on for pressure), but was linearly spaced for mole fraction and temperature features.<sup>56</sup> Also, for all the 3 mixtures tested, the initial training set input points (for all the features) had the same set of values for a fair comparison. The initial training set for the  $P$ - $X$  is given in the Table 1 as an example. As AL progressed more data points were added to the training set. During the AL, the GPs are fit using the complete training set. The test set distribution was not known and was only used for prediction purposes. The test set limits for mole-fraction, and temperature were: [0.02, 0.98] and [200 K, 400 K], respectively. For pressure, the lower limit was  $10^{-6}$  bar for all cases but the upper limit was different for different mixtures. For  $\text{CO}_2$ - $\text{CH}_4$  it was 300 bar, for Xe-Kr it was 200 bar, and for  $\text{H}_2\text{S}$ - $\text{CO}_2$  it was 100 bar. Also a linear distribution of the features was adopted for the test set.

### 2.3 Active learning workflow

The AL workflow that was applied can be divided in these steps:

- Data pre-processing—First the log base 10 transformation of the pressure and temperature (both in  $P$ - $X$  and  $P$ - $X$ - $T$ ) features is performed in the dataset. Then, they are standardized against their mean and standard deviation of the test set. Only the mole fraction feature is linearly scaled to  $-1$  and  $1$ . The standardized version of mole fraction was tested but the linear scaling model worked better, and hence it is adopted. Also the target variable (adsorption  $y$ ) is log (base 10) transformed.
- Model training—The engine of the AL workflow is the GP regression model. A dual GP model was chosen with two

**Table 1** Boundary-informed initial training set grid points for gas mixture adsorption in Cu-BTC MOF for two features ( $P$ - $X$ ) at a fixed temperature of 300 K. Please note, all the data points are same for all three gas mixtures

Pressure (in bar)	Mole fraction	Temperature (in K)
$10^{-6}$	0.02	300
$10^{-5}$	0.20	
$10^{-4}$	0.40	
$10^{-3}$	0.60	
$10^{-2}$	0.80	
$10^{-1}$	0.98	
$10^0$		
$10^1$		
$10^2$		



independent GPs, one for each species in the binary gas mixtures. Both GPs were independently trained with the same input in pressure and temperature (for  $P-X-T$ ), and corresponding mole fraction of the species. Thus, each GP was provided three features for  $P-X-T$  and two for  $P-X$ . GPs are multivariate normal distribution models where each data entry adds a new dimension to the model:<sup>59</sup>

$$f(x) \sim N(\mu(x), k(x_i, x_j)), \quad (1)$$

where  $\mu(x)$  and  $k(x_i, x_j)$  are the mean and covariance matrix of the GP, and  $f(x)$  is the output. The covariance matrix is calculated using kernel function for which many choices are available such as rational quadratic (RQ), Matérn, and radial basis function (RBF). The kernel functions parameters are obtained at the time of fitting the training data. The GP model used in this work is from scikit learn package in Python where the fitting is done by maximizing the log-marginal likelihood function.<sup>69</sup> The L-BGFS-B optimization algorithm is used in this process.<sup>69</sup> Also, multiple kernel functions can be combined together for the GP model, and in this work both double and triple kernel combinations were tested. Out of them, the best performing model was chosen for the final fit. Here is an example of the RBF kernel function with only one parameter, *i.e.* length-scale. The  $d(x_i, x_j)$  here is the Euclidean distance ( $=\|x_i - x_j\|$ ) between the two points:

$$k(x_i, x_j) = \left( -\frac{d(x_i, x_j)^2}{2l^2} \right). \quad (2)$$

Also, an  $\alpha$  regularization term was added to the covariance matrix with a value of  $10^{-4}$  for  $\text{CO}_2\text{-CH}_4$  and  $\text{H}_2\text{S-CO}_2$ , while  $10^{-5}$  for  $\text{Xe-Kr}$ . This is a constant which is added to the diagonal of the covariance matrix to provide an uncertainty threshold so that the data is not overfitted. Please refer to Fig. S3 in the ESI† for further details.

• **Model prediction and convergence criteria**—After the training is complete, the test set is passed through the trained GP models for prediction. For the binary mixtures, we obtain two GP outputs ( $y_1$  and  $y_2$ ), which are scaled back to adsorption by taking the inverse-log of these outputs. Also, the GP gives us the uncertainty distribution in the prediction for each test point,  $\sigma_n$  which is obtained from the covariance matrix. The  $\sigma_n$  is then used to find the most uncertain region in the test set, which shows which areas to actively sample in the next iteration and add to the training set. However, before sampling, we calculate a perceived accuracy (PAC) term which is the stopping criterion for the AL protocol. We define the PAC for adsorption for species  $i$  in a mixture as:

$$\text{PAC}_i = 100 \times \frac{X_+}{X_+ + X_-} \quad (3)$$

$$\text{If at } X_{n_i}, \left| \frac{\sigma_{n_i}}{y'_{n_i}} \right| \leq \beta_i, \text{ then, } X_+ = X_+ + 1 \text{ else, } X_- = X_- + 1 \quad (4)$$

This PAC value is the fraction of points in the test set whose GP relative errors are above a desired relative error threshold. Thus, PAC is a measure of the performance ‘perceived’ by the GP model, which it calculates by counting the number of predictions which fall under a desired relative error limit. In eqn (3) and (4),  $\sigma_{n_i}$  and  $y'_{n_i}$  are the GP-predicted uncertainty and adsorption value (log) associated with the test point  $X_{n_i}$ . Therefore, the concept of PAC is first introduced in this work and has potential to be used for any AL based tasks. This parameter was inspired from the use of the term accuracy in regular classification tasks.<sup>70</sup> Accuracy in a classification task is defined as the ratio of correctly classified test cases to total number of test cases. In classification tasks, the accuracy is determined with respect to ground-truth data. Here a similar concept is used but it is applied to a regression problem (adsorption uptake prediction) while using the  $\beta_i$  threshold as a cut-off for determining PAC. This is a different use of the accuracy measure which comes from GP models during the prediction phase and is not produced from comparing the model prediction with the ground-truth (as is done for a regular classification task). The threshold value  $\beta_i$  is user-defined and can be set on the basis of the desired performance the user needs. Also, the  $\beta$  values were kept same for the all the species in mixture. We had  $\beta$  set to 2% for the  $P-X$  feature space, while it was set to 5% for AL in the  $P-X-T$  space. This was done since the test set in the  $P-X-T$  was much sparser than that of  $P-X$  one ( $21 \times 11 \times 11$  points in the  $P-X-T$  feature space, compared to  $51 \times 49$  points for  $P-X$ ). The test size reduction in the  $P-X-T$  was done to avoid a high computational cost. Including an extra feature while keeping the same test size necessitates the increase in the sparseness of the test set. In scenarios of sparse data, the GP model tends to have large uncertainty while the true performance does not deteriorate or scales down in proportion to the size reduction of the test set. As observed, the final model performance for the same gas mixture for the two cases ( $P-X$  and  $P-X-T$ ) were comparable even though they had different  $\beta$  values (refer Tables 2 and 4). We observed either the individual MREs for the  $P-X-T$  case remained the same as  $P-X$  or they were twice as high in the worst case. Lastly, the PAC was compared to the threshold of convergence, which is set to 90% for all the mixtures for the both the feature-space studies. If 90% of the test set predictions for both the species are less than or equal to  $\beta$ , then the learning is finished and no new point is further sampled. If the PAC policy is not satisfied then the next step is followed.

• **Training set update**—In case any of the two PAC criteria are not satisfied then this protocol is followed. The highest uncertain point in the test set is chosen from both the species (based on  $\sigma_{n_i}$  value) and then the point with maximum  $\sigma_{n_i}$  of the two species is sampled through GCMC. After sampling this point, it is added to the training data set and then the AL restarts. The protocol continues until the PAC condition is satisfied for both the species. Fig. 1 depicts the full AL workflow.

• **Hyperparameters**—Before building the adsorption model, we had to decide on different hyperparameters for a GPR including kernels and regularization parameters. Three different kernel options and their combinations were tested:



**Table 2** The performance summary of the best fit GPs using AL protocol for the 3 gas mixtures after 90% PAC criteria was met in the pressure–mole fraction space ( $P$ – $X$  feature space). Data requirement (in terms of % of ground truth), MRE and  $R^2$  are presented. Also, the species tag number (1 or 2) corresponds to the sequence from left hand side in the mixture name. For e.g. species 1 in  $\text{CO}_2$ – $\text{CH}_4$  will be  $\text{CO}_2$ . The iterations shows the total number of additional points added to the initial training dataset to meet the PAC of 90%

Mixture	Kernel	Iterations	Data requirement (in %)	MRE <sub>(species 1)</sub> (in %)	MRE <sub>(species 2)</sub> (in %)	$R_{(\text{species } 1)}^2$	$R_{(\text{species } 2)}^2$
$\text{CO}_2$ – $\text{CH}_4$	RBF	21	3.001	5.263	5.417	0.986	0.999
Xe–Kr	RQ	11	2.601	6.526	6.394	0.985	0.998
$\text{H}_2\text{S}$ – $\text{CO}_2$	RQ	10	2.561	7.149	7.154	0.982	0.995

rational quadratic (RQ), Matérn, and radial basis function (RBF). We note that the parameters inside all the kernels, such as length-scale  $l$  or  $\alpha$  in RQ are optimized in the GP fitting process to get to the maximum log-likelihood. The only parameter that is not optimized is the  $\nu$  parameter in Matérn, which was set to  $\frac{1}{2}$  since this value gave the best fit as well as consistency in subsequent iterations. Further, the bounds of  $l$  and  $\alpha$  chosen were  $10^{-13}$  to  $10^{13}$ . The equation for RQ and Matérn kernels are:

$$k(x_i, x_j) = \left( 1 + \frac{d(x_i, x_j)^2}{2\alpha l^2} \right)^{-\alpha}, \quad (5)$$

$$k(x_i, x_j) = \frac{1}{\Gamma(\nu)2^{\nu-1}} \left( \frac{\sqrt{2\nu}}{l} d(x_i, x_j) \right)^\nu K_\nu \left( \frac{\sqrt{2\nu}}{l} d(x_i, x_j) \right) \quad (6)$$

The RQ kernel (eqn (5)) has an extra parameter  $\alpha$  when compared to RBF in eqn (2). In eqn (6),  $K_\nu(\cdot)$  is the modified Bessel function, and  $\Gamma(\cdot)$  is the gamma function. Different values of  $\nu$  correspond to different functions.  $\nu$ , as a parameter is used to control the smoothness of the Matérn function. Kernel optimization results for all the different combinations are provided in the ESI.†

• Performance metrics—After selecting the best kernel combination AL fit performance is assessed by various metrics. The GP predicted uncertainties (which are used to find the next point for sampling) are given here for each point.

$$\text{GP relative error in \% (at } x_i) = \frac{\sigma(x_i)}{y'(x_i)} \times 100 \quad (7)$$

$\sigma(x_i)$  and  $y'(x_i)$  are the GP-predicted uncertainty and adsorption value (scaled) associated with the test point of  $x_i$ . Also, a GP mean relative error (MRE) is used to gauge how a current iteration of GP is performing or to what extent the GP “feels” its

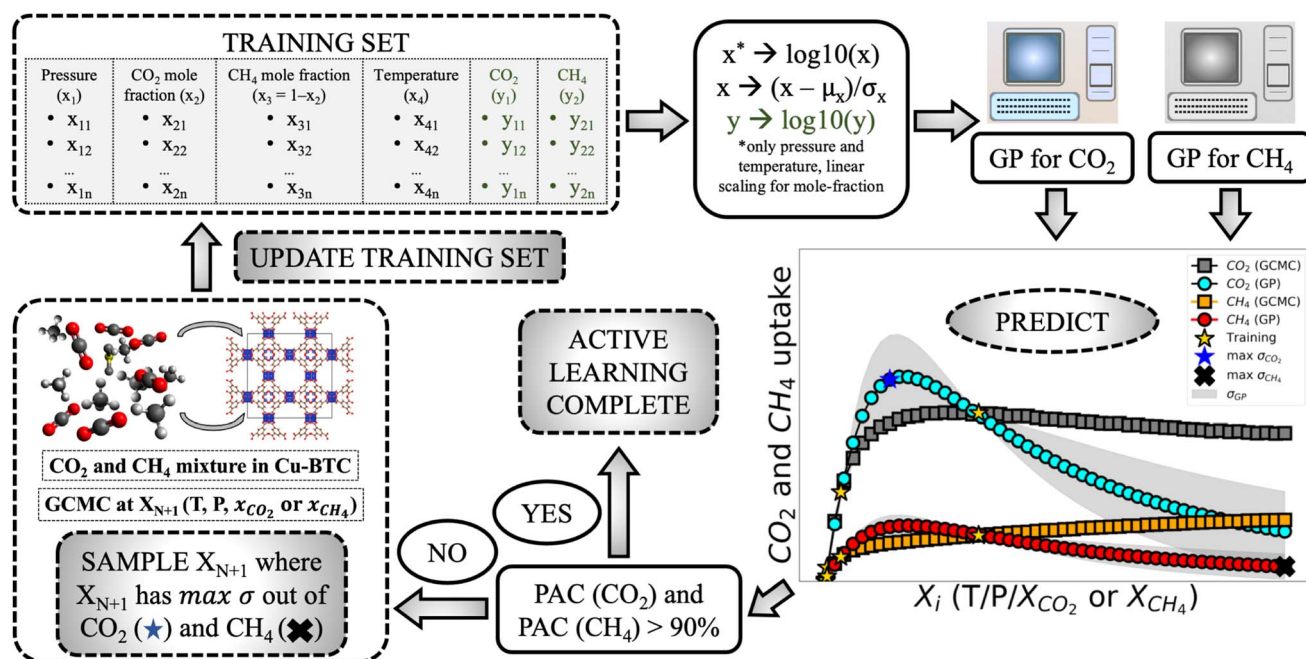


**Fig. 1** Active learning workflow for predicting gas mixture adsorption using Gaussian process regression (GPR). The learning starts from pre-processing the data: pressure and temperature are standardised, while the mole-fraction is linearly scaled to  $-1$  and  $1$  ( $x^* = (x - 1/2) \times (25/12)$ ). Then it is passed through the dual-GPs, one for each species, for training. Please note here only the  $T$ ,  $P$  and the relevant mole-fraction are fed to the GPs (each GP gets three features for  $P$ – $X$ – $T$  and two for  $P$ – $X$ ). Then prediction are done, and the associated uncertainties are extracted. The PACs for both the species are tested for convergence. If any of the PAC criteria is not met, learning continues, and the point with the highest uncertainty is added to the initial training data (out of the two species). The active learning continues until the PAC convergence condition is satisfied.



performance is in aggregate. GP MRE is calculated by averaging GP relative error over all testing points  $n$ , as shown below.

$$\text{GP MRE in \%} = \left( \sum_{i=1}^n \frac{|\sigma(x_i)|}{|y'(x_i)|} \right) \times \frac{100}{n} \quad (8)$$

The next metric is the mean relative error (MRE) where the GP-predicted adsorption ( $Y_{\text{GP-predict}}$ , scaled back from  $y'$ ) is compared with GCMC data ( $Y_{\text{GCMC}}$ ) for all points in the test set and their average is calculated.

$$\text{MRE in \%} = \left( \sum_{i=1}^n \left| \frac{Y_{\text{GP-predict}}(x_i) - Y_{\text{GCMC}}(x_i)}{Y_{\text{GCMC}}(x_i) + \varepsilon} \right| \right) \times \frac{100}{n} \quad (9)$$

The  $\varepsilon (=10^{-3})$  is added to the denominator to avoid numerical issues since adsorption in some feature spaces can reach 0. The same equation is used to find MRE with respect to IAST predictions in Table 5. Only  $Y_{\text{GCMC}}$  is replaced by uptake predictions by the IAST-Langmuir model in the mixture space.

AL was performed for both the  $P$ - $X$  and  $P$ - $X$ - $T$  feature spaces. The major differences for these two cases and the three binary gas mixtures are listed here:

- The points included in the initial training dataset for  $P$ - $X$  are  $9P \times 6X$  (=54 points) and  $5P \times 6X \times 3T$  (=90 points) for  $P$ - $X$ - $T$ . Details are shared in Tables 1 and 3. A detailed discussion for this difference is provided in the  $P$ - $X$ - $T$  results section.

- `n_restart_optimizer`: This was set to 100 for  $P$ - $X$  and 1000 for  $P$ - $X$ - $T$ . This parameter is number of restarts of the L-BGFS-B algorithm while training a GP. The higher the number of restarts, it increases the chances for the GP of finding the kernel parameters which maximizes the log-maximum likelihood function.

- $\alpha$  (the regularization parameter) =  $10^{-4}$  for  $\text{CO}_2$ - $\text{CH}_4$  and  $\text{H}_2\text{S}$ - $\text{CO}_2$ , and  $10^{-5}$  for  $\text{Xe}$ - $\text{Kr}$  (same for both  $P$ - $X$  and  $P$ - $X$ - $T$ ). The parameter was selected from testing on initial training data. More information is shared in the ESI.†

- Kernel combination tested for  $P$ - $X$  feature-space were single ( $k_1$ ) and double additive kernels ( $k_1 + k_2$ ). For  $P$ - $X$ - $T$ , all the permutations of single, double, and triple additive kernels ( $k_1 + k_2 + k_3$ ) were tested. This made a total of 9  $\left( = \sum_{i=1}^2 3^i \right)$

combinations for  $P$ - $X$  and 39  $\left( = \sum_{i=1}^3 3^i \right)$  for  $P$ - $X$ - $T$ . The details of kernel evaluation and results are provided in the ESI.†

- The  $\beta$  value, the relative error constraint which classifies the confident and under-confident regions of the GP for PAC calculation, is 5% for  $P$ - $X$ - $T$  while kept 2% for  $P$ - $X$ .

## 3 Results and discussion

### 3.1 $P$ - $X$ feature space

In the  $P$ - $X$  feature space, the best kernel for  $\text{CO}_2$ - $\text{CH}_4$  mixture was a single RBF. The model based on RBF kernel was chosen as the final surrogate for  $\text{CO}_2$ - $\text{CH}_4$ . In Fig. 2, the GP-predicted adsorption isotherms for three  $X_{\text{CO}_2}$  values are compared with GCMC data. The training points (shown in the star marker)

indicate points GPs were trained on, and here in Fig. 2a we observe that the GP predictions are far from the GCMC and very high uncertainty ( $\sigma_{\text{CO}_2(\text{GP})}$ ). In Fig. 2b, the AL adds a new training point to the training set (based on the highest uncertainty between  $\text{CO}_2$  and  $\text{CH}_4$  uptake) and we find a significant improvement in the adsorption isotherms. This first point added to the training set is at the feature of [ $p = 300$  bar,  $X_{\text{CO}_2} = 0.86$ ]. Thus the uncertainties and predictions of the isotherms at the mole-fraction of 0.80 and 0.50 values show high improvement compared to that of 0.20. Further, the region of high uncertainty also shifts to that of low mole-fraction isotherms. Subsequent additions of data points to training set continues this improvement, as shown by plots (c) and (d) with reduced uncertainty  $\sigma_{\text{CO}_2(\text{GP})}$  and closer agreement of  $y_{\text{CO}_2(\text{GP})}$  with GCMC. Also, out of 49 isotherms (one each  $X_{\text{CO}_2}$ ), only 3 representative isotherms are shown here. We find that out of the 10 points that are added, only a single point belonging to this sub-region was added to the training set (refer plot (d)) training point marked at 300 bar and  $X_{\text{CO}_2} = 0.20$ ). However, since training points added to adjacent regions improves performance, we find a consistent improvement in performance in the regions shown here. Lastly Fig. S2 of the ESI† compares the error heat maps of GP-predicted relative error and absolute relative error for these stages of AL. There we also observe that adding a new point to the training set improves the error maps and the GP-predicted error map starts to converge to the true relative error. For the  $\text{CO}_2$ - $\text{CH}_4$  mixture case, only up to 10 plus the initial training points are shown here. The AL continues further, adding 21 more points to the training set to reach an accuracy of 90% for both the GPs (see Table 2).

In Fig. 3, the progression of the AL protocol (up to 500 iterations) for  $\text{CO}_2$ - $\text{CH}_4$  with the RBF kernel is shown. The GPs meet the desired PAC limit quickly with only 21 additional iterations ( $\approx 3\%$  of the ground truth data). However, the PAC in subsequent iterations fluctuates. This is because new samples added to the training data often leads to increase in GP uncertainty. This happens because with addition of new data the GP algorithm updates its predictions and learns about regions where its earlier predictions were wrong. The algorithm thus updates the uncertainties and that is why with more iterations the gap between MRE and GP-MRE starts to reduce. Only when few more samples are added, an improvement as well as stability in the PAC trend is observed. Also, the fluctuations in the MRE parameter is about 1–2%, which indicates these variations are not as pronounced for MRE as it is for the PAC. This also shows that the newly introduced PAC parameter is quite sensitive to the GP-predicted uncertainty distribution. However, a high PAC does result in low MREs and for all the cases tested (three mixtures as well as the two different feature-spaces), a high PAC provided very good fits. Thus, a high-enough PAC ensures a low MRE, which allows to employ PAC as a policy to stop the learning when the criteria is met for both species (refer to Tables 2 and 4 for other gas mixtures and for  $P$ - $X$ - $T$  feature space). Also, PAC carries additional advantages compared to maximum relative error threshold criteria, which was used for pure components in our earlier work.<sup>56</sup> Some of the reasons of using PAC are listed below:



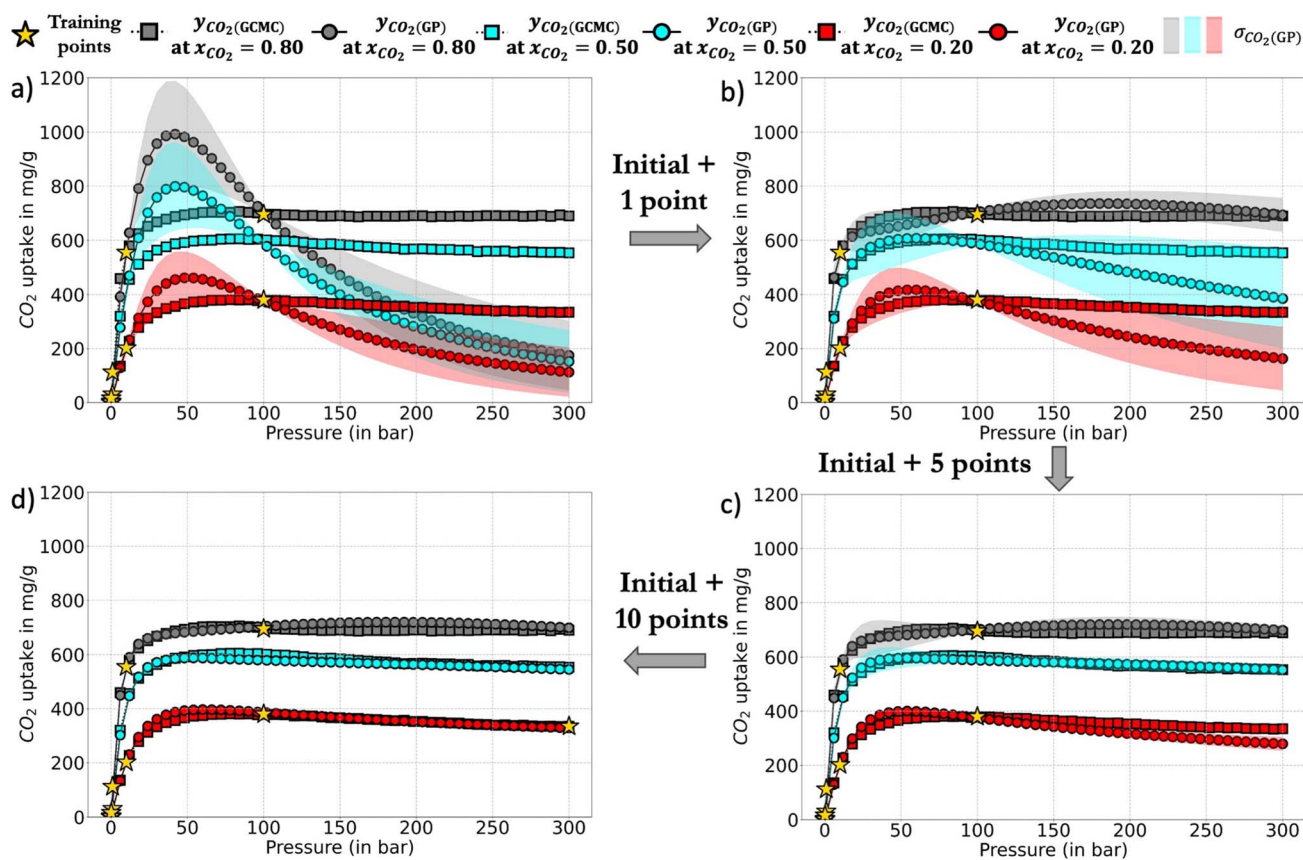


Fig. 2 Comparison of GP predicted CO<sub>2</sub> uptake in Cu-BTC with GCMC in the CO<sub>2</sub>-CH<sub>4</sub> mixture for the CO<sub>2</sub> mole-fractions of 0.80, 0.50 and 0.20 at *P*-*X* phase at 300 K. The progression are shown for (a) initial training data only (= 54 point training set), (b) 1-point + initial training data (=55 point training set), (c) 5-points + initial training (=59 point training set), and (d) 10 points + initial training (=64 point training set). These plots illustrate this: as the AL algorithm continues to add new training points, the gap between GP predictions and ground truth significantly reduces. Further, the uncertainty of the GPs (shown as shaded regions above) also improves. The corresponding GP-predicted relative error maps and the relative error maps are shown in Fig. S2 of ESI.†

• PAC is a fractional quantity (reported in %) of the GP's perceived prediction performance. Therefore, it does not depend on the absolute value of the GP relative error ( $\sigma_n/y$ ) or on the absolute standard deviations  $\sigma_n$ . Depending on the system one is investigating, the distribution of  $\sigma_n$  could be skewed for some regions and hence taking a maximum relative error or even a mean of relative errors or a mean of  $\sigma_n$  itself could pose a problem in determining the cut-off values. Since PAC is a fraction and works on aggregate performance, the same cut-off could work for many diverse systems.

• Due to the fractional nature of the PAC, it can be applied to multiple species (or multiple GPs) with the same cut-off limit. Therefore, it could help to scale the algorithm to multi-output problems.

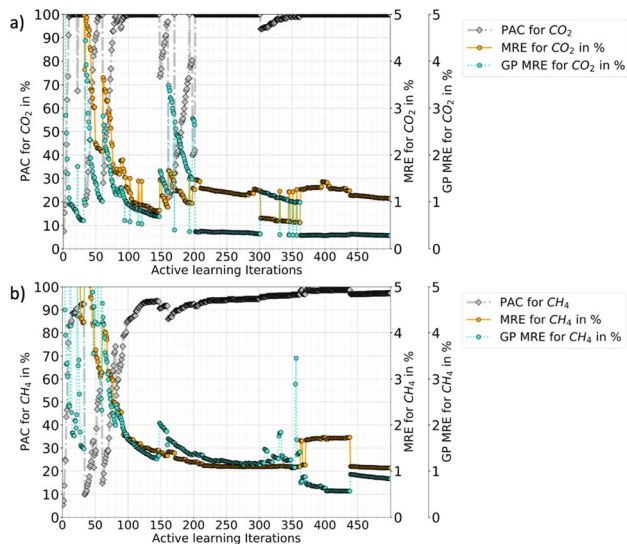
• For mixture adsorption systems (three different mixtures in Cu-BTC, up to 3 features), it was empirically observed that an PAC cut-off of 90% ensures MREs finish within 11% and a  $R^2$  close to one. However, one may need to tune the  $\beta$  parameter.

Fig. 3 also shows that the GP for CO<sub>2</sub> takes more iterations to stabilize than CH<sub>4</sub> (CO<sub>2</sub> PAC stabilizes around 200 iterations while CH<sub>4</sub> at around 100). This happens because the CO<sub>2</sub> adsorption in the mixture has an increasing and then

decreasing trend at low-concentration of CO<sub>2</sub> and eventually follows a type-I adsorption trend at medium to high-CO<sub>2</sub> concentrations (refer Fig. 5). This behaviour was also reported by Tan and coauthors, where they studied mixture adsorption of polar and non-polar gases in carbonaceous nanopores.<sup>71</sup> This feature space where CO<sub>2</sub> adsorption is high at low pressure, corresponds to the synergistic zone where electrostatic interaction of CO<sub>2</sub> with the MOF is stronger. The adsorbates with stronger inter-molecular interactions accumulate near the adsorbent surface and continue to adsorb, out-competing the other gas with weaker adsorbate-adsorbate interaction. However, as pressure is increased CH<sub>4</sub> begins to replace CO<sub>2</sub>. Thus, these two effects results in very different isotherms for different feature space regions. Hence in the CO<sub>2</sub>-CH<sub>4</sub> mixture, the CO<sub>2</sub> uptake is a difficult target variable to learn (compared to CH<sub>4</sub>), requiring more iterations for stabilization.

The relative error heat maps when the PAC conditions are met are reported in Fig. 4, which shows relative error (with respect to GCMC) for each point of the *P*-*X* grid for both species. In this figure, the errors are higher when CO<sub>2</sub> is at a lower concentration (or CH<sub>4</sub> concentration is high). This corresponds to the range of  $X_{CO_2} = 0.02$  to 0.20. Following this, the





**Fig. 3** Active learning progression plots for a single RQ kernel (a)  $\text{CO}_2$  and (b)  $\text{CH}_4$ . In the right hand side, mean relative error (MRE) and Gaussian process mean relative error (GP-MRE) is shown, while the left hand side shows the PAC criteria. This plot compares the perceived performance by the GPs for each species with the true performance along with iterations. As seen in subsequent iterations of the learning, the MRE (true error with respect to the ground truth) converges with the GP MRE. However, with a PAC threshold of 90%, the AL process will finish much earlier than the desired performance. This plot shows if the AL was to progress beyond the cut-off of PAC limit, how the performance would be in the following iterations.

adsorption plots in Fig. 5 are also shown, which compares GP-predicted adsorption with GCMC (ground truth) and IAST predictions, for three-different features of the  $\text{CO}_2$ - $\text{CH}_4$  mixture (at the state when PAC constraints are met). First, in Fig. 5a, we

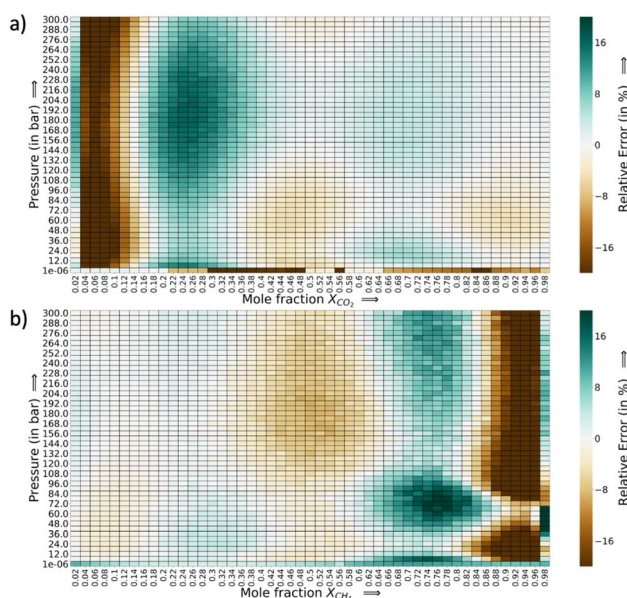


**Fig. 4** Relative error heat maps at the 90% PAC cut-off for  $\text{CO}_2$ - $\text{CH}_4$  mixture, (a)  $\text{CO}_2$  and (b)  $\text{CH}_4$ . The region of  $X_{\text{CO}_2} = 0.02$  to  $0.30$  ( $X_{\text{CH}_4} = 0.70$  to  $0.98$ ) have the highest errors. The model under-predicts adsorption of  $\text{CO}_2$  at  $X_{\text{CO}_2} = 0.02$  to  $0.14$ , and then over-predicts from  $0.14$  to  $0.30$ .

find that GP-predicted  $\text{CO}_2$  uptake is under-predicted compared to the GCMC data. For compositions beyond  $X_{\text{CO}_2} = 0.10$ , the GP starts to over-predict uptake. Then after the value of  $X_{\text{CO}_2} = 0.20$ , the GP fit for  $\text{CO}_2$  has good agreement with the GCMC data. Comparing the GP predictions with IAST, we see it fails to capture the trend completely at low to mid concentrations of  $\text{CO}_2$ . While comparing the performance of GP-predicted uptake for both the species, it performs far better than IAST predictions. Only at high values of  $X_{\text{CO}_2}$  ( $>0.80$ ), does IAST perform well and closely follows the GCMC data. Also, at the low concentration of  $X_{\text{CO}_2}$  ( $0.02$ - $0.20$ ), IAST has high absolute deviation from GCMC and fails to capture the increasing trend of the  $\text{CO}_2$  adsorption. In this range, IAST predicts a type-I isotherm for  $\text{CO}_2$ , while an increase and then decreasing trend for  $\text{CH}_4$ , both of which are far from the ground truth. In contrast, the GP predicted isotherms are consistent with the GCMC data, despite some absolute deviations, there is good agreement with the adsorption trends from GCMC.

The error maps and adsorption plots (compared with GCMC and IAST predictions at the PAC of 90% state) for  $\text{H}_2\text{S}$ - $\text{CO}_2$  and  $\text{Xe}$ - $\text{Kr}$  are provided in the ESI† and they show very similar behavior to that of  $\text{CO}_2$ - $\text{CH}_4$  at the PAC cut-off of 90% (Fig. S5-S8†). Though there are slight differences observed, the final GP fits of  $\text{Xe}$ - $\text{Kr}$  at lower  $\text{Xe}$  concentration are relatively better than  $\text{CO}_2$ , while in the case of  $\text{H}_2\text{S}$ - $\text{CO}_2$ , the GP-GCMC errors are more distributed throughout the feature space. Also, the IAST predictions for  $\text{Xe}$ - $\text{Kr}$  as well for  $\text{H}_2\text{S}$ - $\text{CO}_2$  show large deviations with respect to the GCMC data except at high  $\text{Xe}$  and  $\text{H}_2\text{S}$  compositions. Thus, like the  $\text{CO}_2$ - $\text{CH}_4$  mixture, GP predictions outperform IAST and show similar trends to the GCMC data even when there is a high relative error. IAST fails to capture the trends and has high errors for the majority of the feature space. From the adsorption plots for all the three mixtures, it can be concluded that the species which is more attracted to the Cu-BTC MOF shows high error at low concentration. Since these species ( $\text{CO}_2$ ,  $\text{Xe}$ , and  $\text{H}_2\text{S}$ ) are more attracted to the Cu-BTC structure they can replace the other one quickly as the concentration is increased. This makes it harder for the GP to capture this rapid change when it moves along the small mole-fraction of the more dominant species. This is one of the pitfalls of the PAC protocol that it may not ensure a perfect fit with GCMC at the 90% cut-off. Hence, one has to balance out the need for a model which is accurate with respect to GCMC at all features ranges but might have errors at certain sections/ranges of the test set or one can let the AL continue to 95% or 99%, so that the model is confident at all feature spaces.

In Table 2, different performance indicators for the GP models are summarized when AL is terminated for the  $P$ - $X$  feature space. Since the initial training set (54 points) was kept the same for all gas mixtures, the number of initial training datapoints is also added to calculate the data requirement parameter, which is given below.

$$\text{Data requirement} = \frac{N_{\text{initial training set}} + N_{\text{Iterations to 90\% PAC}}}{N_{\text{ground truth}}} \times 100 \quad (10)$$



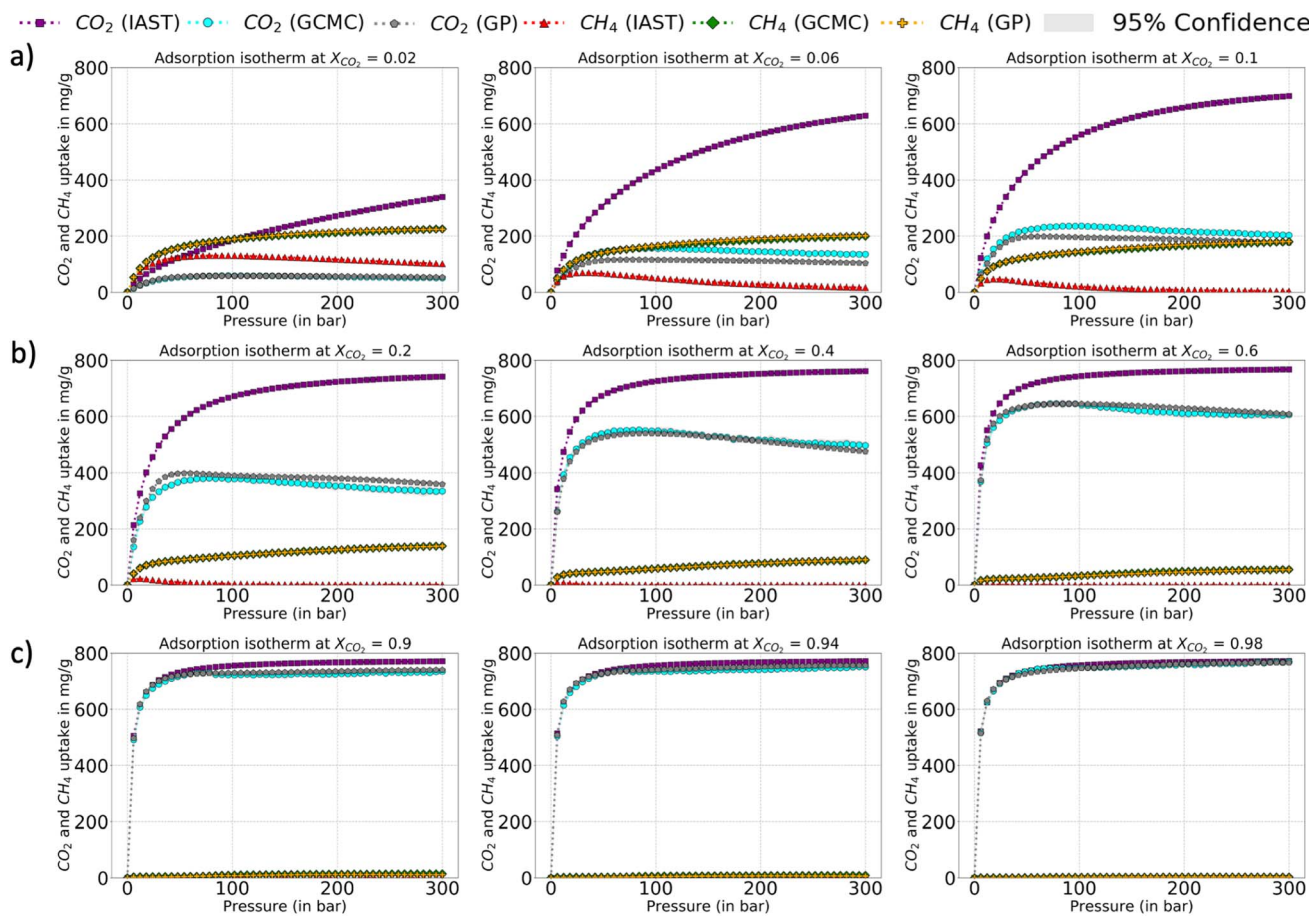


Fig. 5 Adsorption plots of both CO<sub>2</sub> and CH<sub>4</sub> using the RBF kernel in the CO<sub>2</sub>-CH<sub>4</sub> gas mixture after 21 training points are added to initial training set (when 90% PAC criteria is met). The ground truth data is the GCMC predictions which is compared with GP-predictions (at the PAC cut-off of 90%), along with IAST predictions. The plots follows these regions of the mixture: (a) low concentration of CO<sub>2</sub> ( $X_{\text{CO}_2} = 0.02, 0.06, \text{ and } 0.10$ ), (b) medium-concentration of CO<sub>2</sub> ( $X_{\text{CO}_2} = 0.20, 0.40, \text{ and } 0.60$ ), and (c) high-concentration of CO<sub>2</sub> ( $X_{\text{CO}_2} = 0.90, 0.94, \text{ and } 0.98$ ).

Thus, the data requirement is the fraction of total data provided to the GPs to reach the cut-off of 90% PAC for both the species. The other parameters are the MREs and correlation coefficient for both the species. In Table 2, the data requirement is found to be small (within 3% of ground truth) for the 3 mixtures. The MREs for all the species are also good, around 5–7% for the three mixtures. The last quantity,  $R^2$ , is close to one ( $\sim 0.98$ – $0.99$ ) for all the species, showing that the GP captures the adsorption trend quite well. Thus, in this section it is shown how AL can be used to build reliable surrogate models which work for different gas mixtures and can give a satisfactory performance. With these results it is demonstrated that the cut-off of 90% PAC gives low relative errors and provides good agreement with the ground truth data. This AL termination protocol can thus balance the number of iterations or simulations one needs to conduct *versus* the performance of the model.

### 3.2 $P$ - $X$ - $T$ feature space

This section deals with AL in the  $P$ - $X$ - $T$  feature space. As stated before, the initial training set size in this  $P$ - $X$ - $T$  study is

increased to 90 points. This is done because with three features the initial training dataset has to include a new feature: temperature. The distribution for initial training set  $P$ - $X$ - $T$  is  $5P \times 6X \times 3T$  (as shown in Table 3). This particular distribution is arranged so that the most sensitive features gets a high share of points in the initial dataset, hence only 3 points are for temperature while 6 points are given for the mole fraction. Also, the magnitude of initial training input points are kept equal for all three gas mixtures for a fair comparison between mixtures (just like the  $P$ - $X$  case). The kernel selection plots for  $P$ - $X$ - $T$  case

Table 3 Boundary-informed initial training data grid points for gas mixture adsorption in Cu-BTC MOF for three features ( $P$ - $X$ - $T$ )

Pressure (in bar)	Mole fraction	Temperature (in K)
$10^{-6}$	0.02	200
$10^{-4}$	0.20	300
$10^{-2}$	0.40	400
$10^0$	0.60	
$10^{+2}$	0.80	
	0.98	



is provided in the ESI.† For CO<sub>2</sub>-CH<sub>4</sub> mixture, the triple-RBF kernel was selected for the AL (see Fig. S9† for details). The desired PAC was met after 64 iterations of active learning, which

amounts to a data expenditure of 6.61% (Table 3). The MREs for both species had a slight difference: CH<sub>4</sub> has an MRE of 9.25% whereas CO<sub>2</sub> has 5.46%. These are good results considering only 6.61% of data is used for training from the ground truth.

Fig. 6 shows the progression of AL for triple RBF kernel for CO<sub>2</sub>-CH<sub>4</sub> mixture in the  $P$ - $X$ - $T$  feature space (up to 500 iterations). Here, the fluctuations in the PAC value is less compared to the  $P$ - $X$  counterpart. Also, there are sharp drops in PAC for CH<sub>4</sub> which reflects that with new data the GP model's uncertainty is increased in the prediction, until it gets additional data points to reduce the uncertainties. Like  $P$ - $X$ , the PAC cut-off was set to 90% and the model reaches this threshold relatively slowly compared to  $P$ - $X$ . Fig. 6 also shows if the learning had continued beyond the cut-off of 90%, around 400 total iterations are needed to meet the 95% PAC threshold. This means that around 20% of the ground truth has to be included in the training set and this would have resulted in an MRE of 2% and 3% for CO<sub>2</sub> and CH<sub>4</sub>, respectively. This finding shows the cost-performance ratio of the learning process and demonstrates that adding more data leads to a slow improvement in the model. Hence, an early cut-off of 90% can provide a 'good-enough' model, instead of spending 20% of ground-truth (400 more iterations) to get only a 5% gain in the PAC or 2–4% drop in MREs.

The error heat maps for each mole fraction of CO<sub>2</sub> and CH<sub>4</sub> (at the AL state when PAC criteria is met) are provided in Fig. 7 and 8. For CO<sub>2</sub>, the highest error region corresponds to  $X_{\text{CO}_2} = 0.116$ , followed by  $X_{\text{CO}_2} = 0.308$ . The rest of the region has very low relative errors, irrespective of the pressure or temperature values. Also, the errors are marginally high in the low

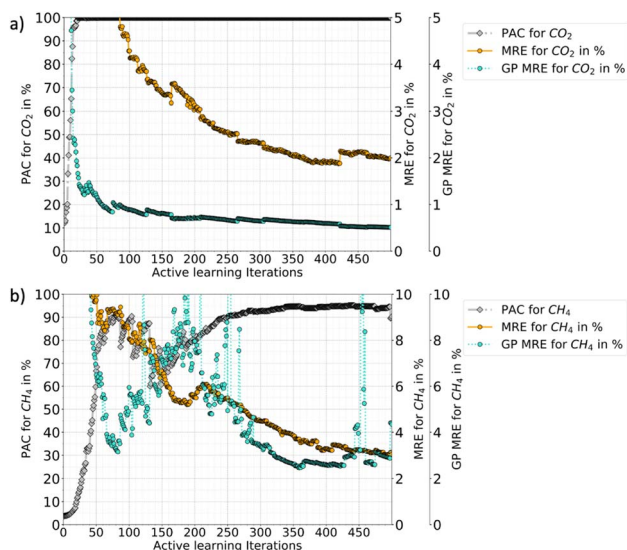


Fig. 6 Active learning progression plots for a triple-RBF kernel for  $P$ - $X$ - $T$  feature space (a) CO<sub>2</sub>, and (b) CH<sub>4</sub>. This plot compares the perceived performance by the GPs for each species with the true performance along with iterations. As seen with subsequent iterations of the learning, the MRE (true error with respect to the ground truth) converges with the GP MRE. However, as the PAC threshold is set to 90%, the AL process will finish much earlier for a desired performance. This plot show if the AL was to progress how the performance would be in the following iterations.

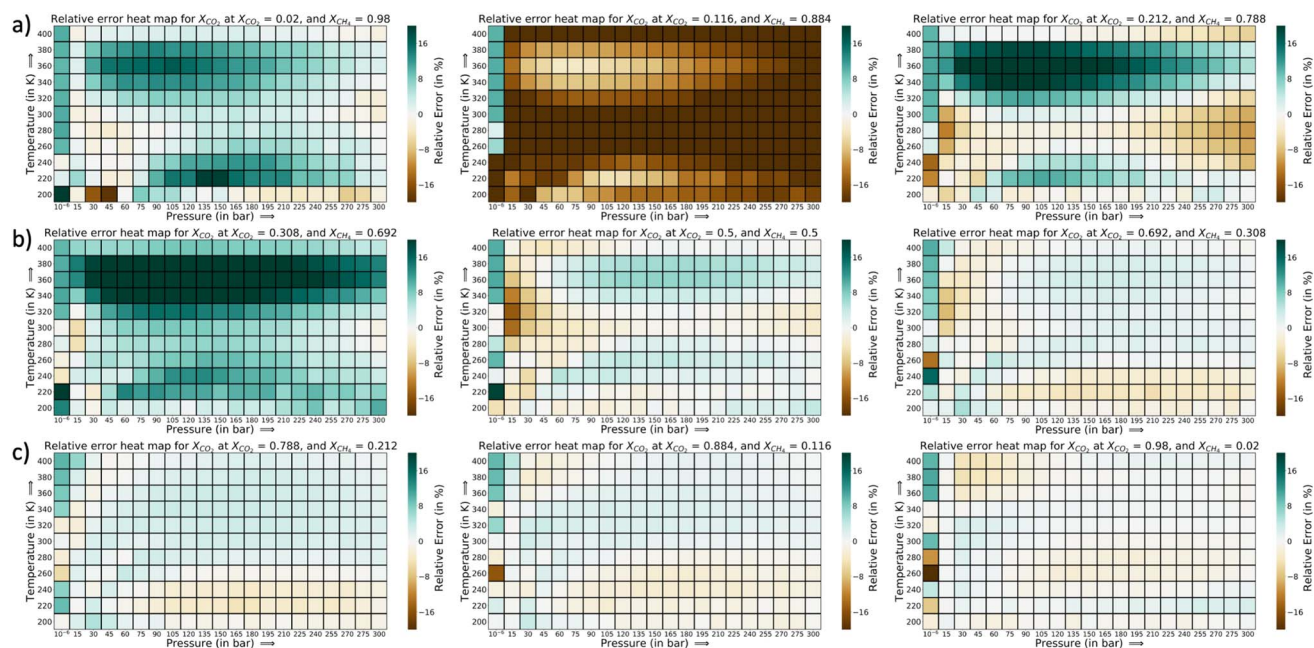
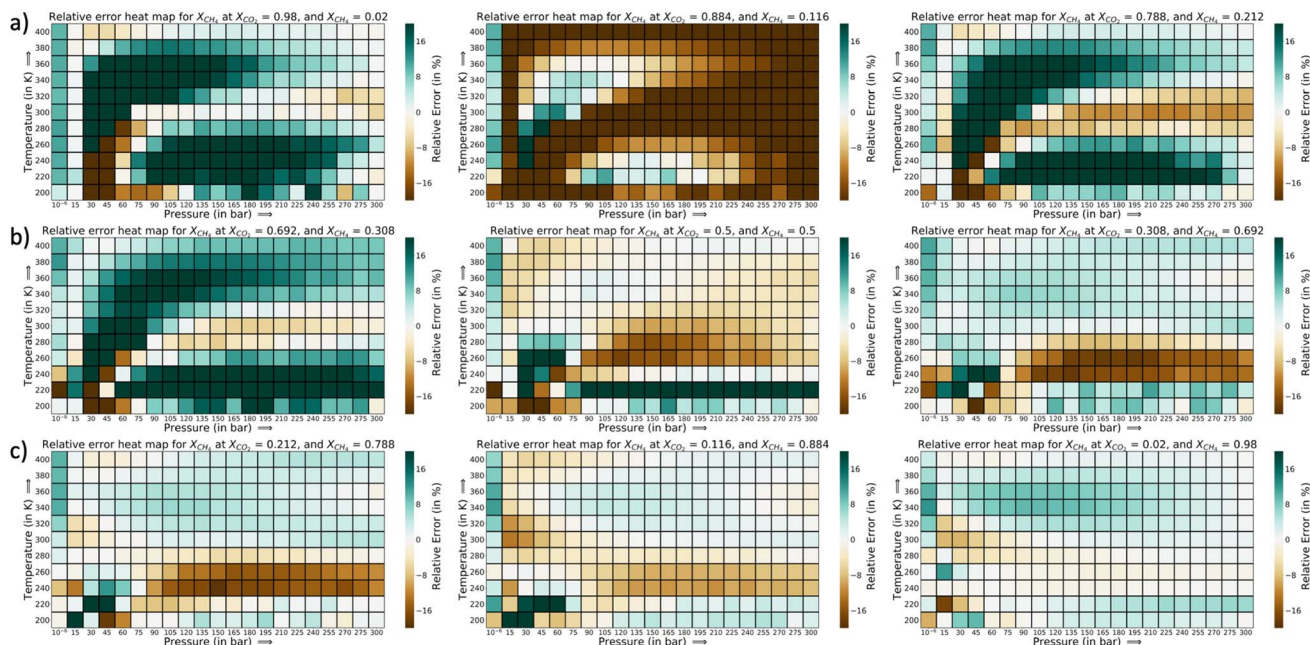


Fig. 7 Relative error heat maps at the 90% PAC cut-off for CO<sub>2</sub> in the CO<sub>2</sub>-CH<sub>4</sub> mixture with triple-RBF kernel, (a)  $X_{\text{CO}_2} = 0.02$ , 0.116, and 0.212, (b)  $X_{\text{CO}_2} = 0.308$ , 0.5, and 0.692, and (c)  $X_{\text{CO}_2} = 0.788$ , 0.884, and 0.98. We find the region of  $X_{\text{CO}_2} = 0.116$  ( $X_{\text{CH}_4} = 0.884$ ) having the highest errors for CO<sub>2</sub> uptake, with most errors showing that GP model in under-predicting. After this region, there are some error region for  $X_{\text{CO}_2} = 0.308$ , with slight over-prediction by the GP, compared to GCMC.





**Fig. 8** Relative error heat maps at the 90% PAC cut-off for CH<sub>4</sub> in the CO<sub>2</sub>-CH<sub>4</sub> mixture with triple-RBF kernel. (a)  $X_{\text{CH}_4} = 0.02, 0.116,$  and  $0.212$ , (b)  $X_{\text{CH}_4} = 0.308, 0.5,$  and  $0.692$ , and (c)  $X_{\text{CH}_4} = 0.788, 0.884,$  and  $0.98$ .

temperature range. At the highest temperature of 400 K, the errors are very small. In Fig. 8, a similar trend in the error distribution of CH<sub>4</sub> is observed. However the errors are distributed more than CO<sub>2</sub> from the feature value of  $X_{\text{CH}_4} = 0.02$  to  $X_{\text{CH}_4} = 0.50$ . In this range of CH<sub>4</sub> mole-fraction, the CH<sub>4</sub> uptake is small which can explain the rise in the relative error. As the adsorption plots shows, the GP-predictions strongly correlates with the GCMC data. Further in this plot, the errors are slightly high as temperature is increased. This is in the opposite direction of CO<sub>2</sub> relative error trend. As temperature increases, CH<sub>4</sub> adsorption falls and the relative error spikes because of the smaller  $y_1$  in the denominator. However with CO<sub>2</sub>, with rise in temperature the synergistic effect weakens at low CO<sub>2</sub> mole-fraction and the increase and decrease trend of the CO<sub>2</sub> isotherm shifts to higher concentration of CO<sub>2</sub>. Thus, the GP is able to capture that trend well at high temperatures for CO<sub>2</sub>. Fig. S18 and S19† show the adsorption data for these highest relative error region for CO<sub>2</sub> and CH<sub>4</sub>. Thus, through this analysis it becomes clear that errors for each species are very sensitive to the mole fraction and temperature in the  $P$ - $X$ - $T$  phase space.

The corresponding adsorption plots for the region of  $X_{\text{CO}_2} = 0.116$  is provided in Fig. 9a, and through them it is observed that the GP model, in many places, fails to capture the true adsorption values for CO<sub>2</sub>. However, it succeeds in capturing the overall trend of the GCMC, compared with IAST. The IAST trends for both CO<sub>2</sub> and CH<sub>4</sub> across the temperature fails very similarly to the  $P$ - $X$  space. IAST deviates from the GCMC data completely in this region while GP shows moderate relative errors. In Fig. 8, the error heat map for CH<sub>4</sub> is shown. Here the errors are more distributed with mole-fraction compared to CO<sub>2</sub>. Also, the errors are high only in the region when CH<sub>4</sub> is less

than 0.50 mole-fraction. The adsorption plots for these high error region had been added in Fig. S18 of ESI,† where the adsorption isotherm at these high error region of  $X_{\text{CH}_4} = 0.884$  ( $X_{\text{CO}_2} = 0.116$ ) are shown. The CH<sub>4</sub> GP fit follows the GCMC data very closely however has a moderate deviation in absolute value. Also, the CH<sub>4</sub> uptake is very small in these regions which disproportionately increases the MRE values ( $y_2$  being the denominator in MRE calculation). The overall MRE of 9.25% can be thus attributed to region where CH<sub>4</sub> uptake is small. Further in Table 4, the  $R^2$  for CH<sub>4</sub> very close to 1, which shows a very strong correlation of final GP fit with GCMC data. In Fig. S27,† we have also added a comparison plot for the GP-predicted CO<sub>2</sub> and CH<sub>4</sub> uptakes with the experimental data from Hamon *et al.* (obtained from the BISON dataset).<sup>72,73</sup> There also we find a very close agreement of the GP predicted uptakes with experiments for the three different ratios of CO<sub>2</sub> and CH<sub>4</sub> at 303 K.

In Fig. 9b and c, a comparison of the GP fits with highest relative errors is shown along with IAST predictions for the other two mixtures. The figures for these mixtures are included with the same set of input features ( $X_{\text{species } 1} = 0.116,$  and  $T = 200, 240,$  and  $280$  K) which had shown highest relative errors in the error heat maps previously. The highest deviation (compared to GCMC) of IAST predictions comes from the species which has more affinity towards Cu-BTC. Comparing them with the GP predictions, the GPs also have high errors but it does follow the trend of GCMC isotherms (same as  $P$ - $X$  space). Thus, IAST predictions fail again in the mixture states for  $P$ - $X$ - $T$  feature space for the three mixtures. However since GPs have been trained on a fraction of the ground truth, it has the necessary information to generate the adsorption profiles close to GCMC.



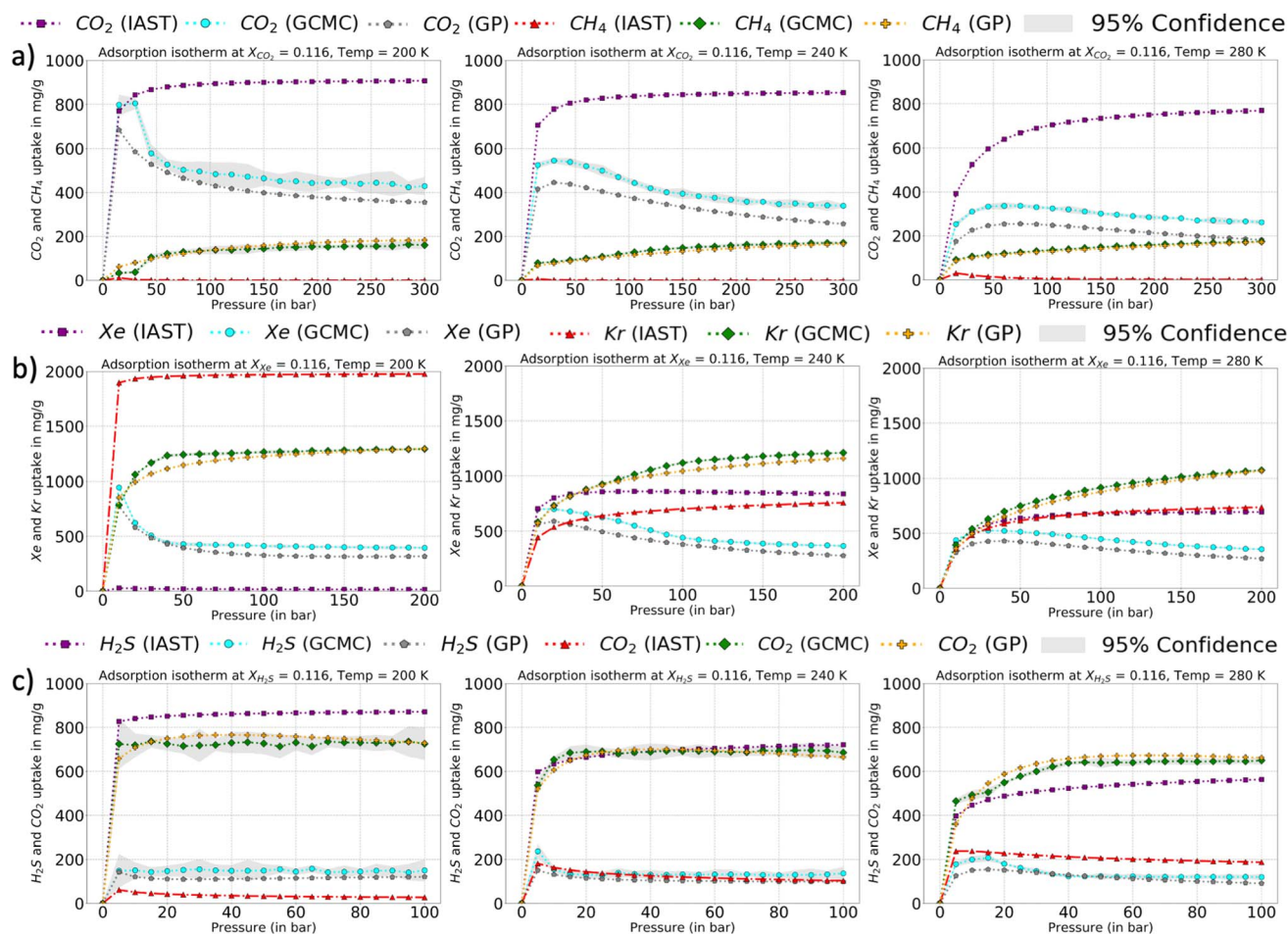


Fig. 9 Adsorption isotherms comparison of GCMC (ground truth), IAST-predicted isotherms, and GP predictions at the 90% PAC cut-off for a few of regions with highest relative errors for all the three mixture, (a)  $X_{\text{CO}_2} = 0.116$  and  $T = 200, 240,$  and  $280$  K, (b)  $X_{\text{Xe}} = 0.116$  and  $T = 200, 240,$  and  $280$  K, and (c)  $X_{\text{H}_2\text{S}} = 0.116$  and  $T = 200, 240,$  and  $280$  K. Also, the IAST prediction fails for species which are more attracted to Cu-BTC ( $\text{CO}_2$ , Xe, and  $\text{H}_2\text{S}$ ) (compared to the second species).

Table 4 The performance summary of the best fit GPs using AL protocol for the 3 gas mixtures after 90% PAC criteria was met in the pressure–mole fraction–temperature space ( $P$ – $X$ – $T$  feature space). Data requirement (in terms of % of ground truth), MRE and  $R^2$  are presented. Also, the species tag number (1 or 2) corresponds to the sequence from left hand side in the mixture name. For e.g. species 1 in  $\text{CO}_2$ – $\text{CH}_4$  will be  $\text{CO}_2$ . Also, the iterations shows the total number of additional points added to the initial dataset to meet the PAC of 90%

Mixture	Kernel	Iterations	Data requirement (in %)	MRE <sub>(species 1)</sub> (in %)	MRE <sub>(species 2)</sub> (in %)	$R^2_{(\text{species } 1)}$	$R^2_{(\text{species } 2)}$
$\text{CO}_2$ – $\text{CH}_4$	Triple-RBF	78	6.611	5.461	9.256	0.988	0.990
Xe–Kr	Triple-RBF	79	6.650	4.850	7.025	0.990	0.990
$\text{H}_2\text{S}$ – $\text{CO}_2$	RQ	51	5.549	8.276	11.682	0.976	0.986

In Table 4, the AL performance for all three mixtures for  $P$ – $X$ – $T$  feature space is shown. All the MREs are in acceptable range of 4–11%, and  $R^2$ 's are close to 1. The data requirement is close to 5–6% with the triple-RBF kernel providing best fit for  $\text{CO}_2$ – $\text{CH}_4$  and Xe–Kr, and a RQ for  $\text{H}_2\text{S}$ – $\text{CO}_2$ . From these results, it is apparent that the GP model does a good job in emulating the adsorption isotherm at different conditions. The only section with moderate errors is the range with small concentration of species with high affinity towards the MOF structure ( $\text{CO}_2$ , Xe,

and  $\text{H}_2\text{S}$ ). Comparing this to IAST performance for the feature-spaces and mixtures (shown in Table 5), we find the errors are very high (varying from 30% to 91.09%). Therefore, the aggregate performance of AL-based isotherms are much better than IAST-based predictions.

The error maps and adsorption plots (for region with highest relative errors) for Xe–Kr and  $\text{H}_2\text{S}$ – $\text{CO}_2$  are provided in Fig. S14 to S23 in the ESI.† A similar trend in error and adsorption isotherms (like  $\text{CO}_2$ – $\text{CH}_4$ ) was observed for Xe–Kr. In that



**Table 5** IAST (based on Langmuir model) predicted isotherms aggregate performance comparison with GCMC uptakes for all the gas mixtures for the two features spaces

Mixture	Features	MRE <sub>(species 1)</sub> (in %)	MRE <sub>(species 2)</sub> (in %)
CO <sub>2</sub> -CH <sub>4</sub>	<i>P-X</i>	53.97	91.09
Xe-Kr	<i>P-X</i>	27.90	50.20
H <sub>2</sub> S-CO <sub>2</sub>	<i>P-X</i>	25.04	28.69
CO <sub>2</sub> -CH <sub>4</sub>	<i>P-X-T</i>	48.26	98.06
Xe-Kr	<i>P-X-T</i>	35.76	46.15
H <sub>2</sub> S-CO <sub>2</sub>	<i>P-X-T</i>	27.93	63.96

mixture, most of the error are in the low concentration of the species with strong affinity to Cu-BTC (Xe for Xe-Kr). For H<sub>2</sub>S-CO<sub>2</sub> the scenario is different as the errors are more distributed in the mole fraction feature space. This is due to the nature of target adsorption distribution in the H<sub>2</sub>S-CO<sub>2</sub> mixture where both the species have a high affinity towards the MOF. Therefore the changes in adsorption isotherm are more distributed and the errors in GP fit too gets extended or flattened out with respect to mole-fraction. This is an interesting aspect of the protocol which demonstrates that the GP can learn diverse target adsorption isotherms with very good performance. In this direction, we have also added correlation plots for all the three mixtures in the ESI, Fig. S23-S25.† These plots show the location of points sampled by the algorithm beyond the initial training set. These plots illustrate that pressure points are more frequently sampled along the boundaries of the test set range. For mole-fraction points we see a similar profile as pressure but there are more points in the middle range than pressure. We see the most uniform sampling along the temperature feature for all the three mixtures.

We also note an interesting observation when looking at the difference in individual species GP performance are compared for all mixtures. In Fig. 10 the mean difference between the species GP-MRE and  $R^2$  are plotted against iterations (calculated cumulatively at interval of ten points). This plot both covers the difference in GP's perceived performance (GP-MRE) and the actual performance (shown by  $R^2$ ) among the species. In this plot, a hierarchy in the GP-MRE and  $R^2$  difference is observed among the three mixtures. CO<sub>2</sub>-CH<sub>4</sub> have the highest mean difference in GP-MRE and  $R^2$ , followed by Xe-Kr, and then H<sub>2</sub>S-CO<sub>2</sub>. In Fig. 10, the differences in GP-MRE and  $R^2$  among the mixtures shows that CO<sub>2</sub>-CH<sub>4</sub> has high difference in the model performance between the two species. This affects both the final performance at the AL termination as well as the total number of iterations required to meet the cut-off PAC. The difference in the individual species perceived performance creates the demand for more ground-truth data to be provided to the model. In Table 4, we observe that CO<sub>2</sub>-CH<sub>4</sub> has higher values of MRE compared with Xe-Kr, while both mixtures take almost the same number of iterations to reach 90% PAC (78 iterations against 79). Again in Table 4, when CO<sub>2</sub>-CH<sub>4</sub> is compared with H<sub>2</sub>S-CO<sub>2</sub>, it has slightly lower MRE, but the latter mixture took significantly less number of iterations to fulfil the PAC criteria. Going back to Fig. 10, we emphasize that CO<sub>2</sub>-CH<sub>4</sub> inter-species model differences is followed by Xe-Kr and H<sub>2</sub>S-CO<sub>2</sub>. Therefore, Xe-Kr and H<sub>2</sub>S-CO<sub>2</sub> are more closer in absolute values for the inter-species model difference than Xe-Kr is to CO<sub>2</sub>-CH<sub>4</sub>. Because the y-axis is shown in the log<sub>10</sub> scale, the relative difference among mixtures looks equal for the three mixtures. Further, when AL results of the *P-X* feature space is taken into account (Table 2), CO<sub>2</sub>-CH<sub>4</sub> again takes twice the number of iterations to reach 90% PAC compared to other two mixtures, while there is only 1-2% reduction is

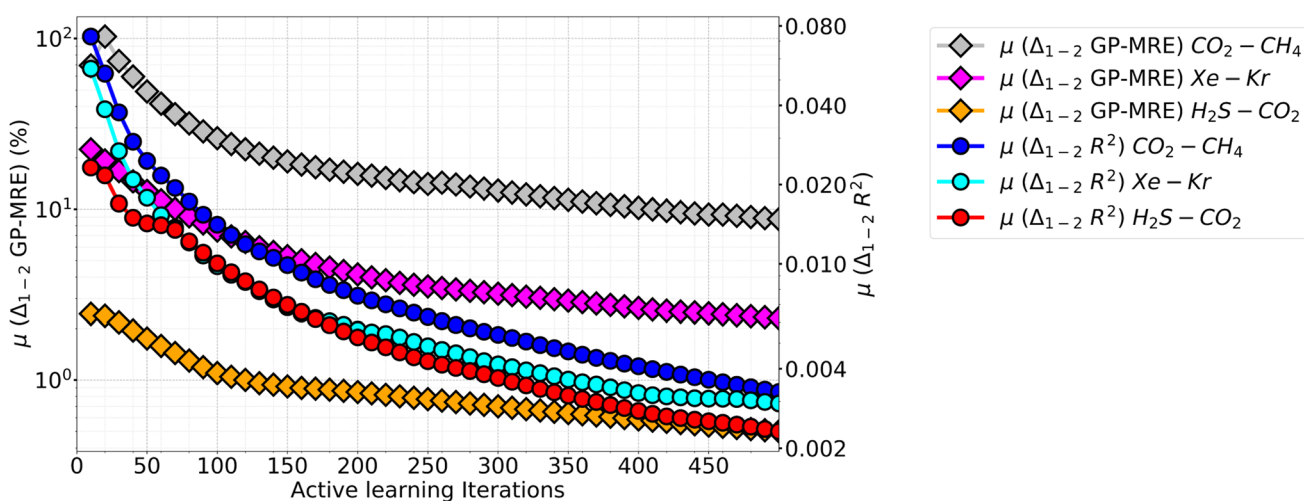


**Fig. 10** Comparison of differences in GP-model performance (shown as the mean of GP-MRE difference between two species) and mean of difference in correlation coefficient ( $R^2$ ) against the number of AL iterations (up to 500). All the three mixtures are included here and the GPs of CO<sub>2</sub>-CH<sub>4</sub> had the most difference in terms of GP-MRE as well as  $R^2$ , followed by Xe-Kr and then H<sub>2</sub>S-CO<sub>2</sub>. Also the mean of difference were taken after an interval of 10 points and all the previous points were included. It is to be noted that CO<sub>2</sub>-CH<sub>4</sub> is quite farther than other two mixtures, only because of the use of log<sub>10</sub> scale, it seems that the difference in the three mixtures are same. Realistically, CO<sub>2</sub>-CH<sub>4</sub> is much farther than other two, while Xe-Kr has slightly higher difference in GP-MRE and  $R^2$  than H<sub>2</sub>S-CO<sub>2</sub>.



observed in the MRE values, while  $R^2$  values are in the same range as other mixtures.

All gases taken together, our results suggest AL performance is affected by the similarities in the intermolecular interactions of species in a given gas mixture. This difference in inter-species model behaviour of the GPs can also be examined *via* the nature of adsorbate species. Out of the five molecules in three mixture base, one is polar ( $\text{H}_2\text{S}$ ) while other four are non-polar ( $\text{CO}_2$ ,  $\text{CH}_4$ , Xe, and Kr). Also, the models of  $\text{CO}_2$  and  $\text{H}_2\text{S}$  have charges in their respective atoms while the models for  $\text{CH}_4$ , Xe, and Kr do not carry charges.<sup>63</sup> Therefore in  $\text{CO}_2$ - $\text{CH}_4$  mixture, both the species exhibit very different adsorbate-adsorbate interactions as well as have differences in their affinity towards the MOF.  $\text{CO}_2$  has much stronger adsorbate-adsorbate interaction as well as strong electrostatic interaction with the Cu-BTC (along with Lennard-Jones interaction). This can be demonstrated by comparing the pure component adsorption of these species. For the pure component adsorption, at 300 bar and 300 K,  $\text{CO}_2$  uptake is  $777.084 \text{ mg g}^{-1}$ , while at those conditions the  $\text{CH}_4$  uptake in Cu-BTC is  $240.84 \text{ mg g}^{-1}$ . This difference in adsorbate-adsorbate as well as adsorbate-MOF interaction translates itself into very different individual adsorption isotherms among these species. Therefore, the AL for individual species progresses very differently in  $\text{CO}_2$ - $\text{CH}_4$ . This is reflected as a disparity in the GP-MRE of individual species and thus affects the choice of the next point to be sampled. In essence,  $\text{CO}_2$ - $\text{CH}_4$  needs more AL iterations to reach the same cut-off PAC. In case of Xe-Kr, their pure component uptakes at 200 bar and 300 K are  $1494.33$  and  $1254.80 \text{ mg g}^{-1}$ , respectively. Lastly, in case of  $\text{H}_2\text{S}$ - $\text{CO}_2$ ,  $\text{CO}_2$  and  $\text{H}_2\text{S}$  at 100 bar and 300 K have an uptake of  $751.93$  and  $631.22 \text{ mg g}^{-1}$ . In the case of Xe-Kr, Xe has a higher uptake ( $1494.33 \text{ mg g}^{-1}$ ) than Kr ( $1254.80 \text{ mg g}^{-1}$ ) as pure components. Since both species are non-polar and noble gases, the difference can be mostly attributed to adsorbate-adsorbate interactions. Therefore, Xe demonstrates a stronger adsorbate-MOF interaction than Kr, and thus there is some disparity in the isotherms, which translates to the difference in model performance, though not in the same order as  $\text{CO}_2$ - $\text{CH}_4$ . Finally, in case of  $\text{H}_2\text{S}$ - $\text{CO}_2$ , the difference in both type of interaction are similar for both adsorbates and hence their respective GP models performance are very close to one another (also refer to Fig. S13†). Thus both these two mixtures have less difference in their inter-species GPs performance as they have similar inter-adsorbate and MOF-adsorbate interaction. Extending this analysis, one can envisage that a mixture of  $\text{CH}_4$  and  $\text{H}_2\text{S}$  would have similar problems like that of  $\text{CO}_2$ - $\text{CH}_4$ . This shows that gas mixtures based on components with similar inter-adsorbate and adsorbate-MOF interaction would have better AL results (in terms of iterations to model performance) than mixtures which have diverse adsorbate-adsorbate and adsorbate-MOF interactions.

## 4 Conclusions

From the analysis of gas mixture adsorption in Cu-BTC, we found that the GCMC isotherms are highly sensitive to mole fraction followed by the changes in pressure and temperature. Depending

on the input feature spaces the isotherm can change from a type-I to a very different trend (first rise and then sharp decline). Thus, non-parametric surrogate models which are flexible and can emulate any target distribution are well suited to capture such trends. As shown in this work by the proposed AL protocol, a model based on GPs can be built to predict mixture adsorption in MOFs. Further, each GCMC simulation point for a gas mixture can take from a few hours to more than a day (based on RASPA calculations). On the other side, GPs only takes a few minutes to train and do the prediction, thus the method could save huge in terms of computational costs. Also, AL-based adsorption predictions are better than IAST predictions, which currently are used for multi-component adsorption prediction. The proposed algorithm has been shown to work for two different feature spaces with three different binary gas mixtures which had varying degree of adsorbate-adsorbate as well as adsorbate-adsorbent interactions. Further, AL doesn't need many training points and only with a fraction of ground truth (3–6%), it provides a very good approximation of the target adsorption. The savings in data, however can vary depending on the mixture system, and also on type and number of features. Though on most occasions, more than 90% savings in data sampling requirement were observed. While in this work only up to three features were tested, it would be interesting to find how the model will perform with more features. From the increase in the data requirement from  $P$ - $X$  to  $P$ - $X$ - $T$  (almost double in % term for each mixture), one can hypothesize that addition of adsorption sensitive features to the test set may increase the requirement of training data if the desired perceived accuracy threshold performance is kept the same as that of low feature space.

In this work, an perceived accuracy parameter was also introduced as a condition for the AL convergence. The parameter was inspired from the accuracy metric used for the classification tasks but here it was slightly modified to capture GP's perceived performance. It was observed that the gain in performance does not necessarily increase proportionally as more data was provided to the model. Therefore it is important to have a condition for convergence which can act as a proxy for the desired performance. One disadvantage of this approach could be that the PAC criteria only ensures an aggregate performance, *i.e.* majority of predictions will be in acceptable range while a small fraction, depending on the PAC limit, may underperform. While in this work singularly large deviations were not observed, given the large option of feature spaces there can be cases where deviations could become significantly large. Further, depending on the application, even moderate deviations cannot be accepted. In this direction, more research is needed to ensure a high performance expectation throughout each domains in the test set, and not just as an aggregate.

A further look could be given on the algorithm recommended sampling process too. In this work, sequential sampling of a single data point was used (only one point per iteration), but there could be methods to sample multiple points in a single iteration. Only concern is to find the policy of batching or the criteria of selecting the collection of points in the next batch. If one considers only the collection of points with highest uncertainty then many of them may fall under the same sub-space of the design space, and addition of multiple points may not bring



the desired benefit one might expect. A recent work by Zavala and team successfully showed two parallel sampling schemes for Bayesian optimization, which shows promising results.<sup>74</sup> One was based on informed partitioning of the input space using the target function. Another was the level-set partition criteria, which used a low-fidelity reference model for approximating the target function and perform the partitioning. Though AL is not an optimization problem, one might test and design novel strategies that could be transferred from these works to an adsorption problem. In another direction, calculating the next set of simulations for multiple pressure points (with other features constant) can also be explored since many MC engines or sometime even laboratory experiments could be more efficient in generating adsorption at a fixed temperature rather sampling at different temperatures. Ultimately, there can be more efficient ways to add training points and build a model with high reliability and performance. Further, the methods can be tuned based on the constraints and leverages of the ground truth evaluation procedure. In essence, there are many frontiers of the AL paradigm that could be explored to reduce computational cost and further better the performance of the surrogate models. Adsorption is a unique physical process and as more MOFs and target applications continue to emerge, it would become difficult to perform experiments to identify a MOF for a certain application. The efficiency and scale-ability of computational methods can prove valuable for these situations.

## Data availability

The code written during this work is available at Github: <https://github.com/mukherjee07/Active-Learning-for-multicomponent-adsorption-in-a-MOF>.

## Conflicts of interest

There are no conflicts to declare.

## Acknowledgements

KM would like to thank the ND Energy's Eilers Family Graduate fellowship. EO would like to thank the Lucy Family Institute for Data and Society. All Authors gratefully acknowledge NSF CAREER Award CBET-2143346. The authors would like to acknowledge the Colón group members, specifically João Dinis Oliveira Abranches and Sanoj, for their helpful feedback on this project. We also thank the Center for Research Computing at the University of Notre Dame for computational resources.

## Notes and references

- M. Kondo, T. Yoshitomi, H. Matsuzaka, S. Kitagawa and K. Seki, *Angew. Chem., Int. Ed. Engl.*, 1997, **36**, 1725–1727.
- O. K. Farha, I. Eryazici, N. C. Jeong, B. G. Hauser, C. E. Wilmer, A. A. Sarjeant, R. Q. Snurr, S. T. Nguyen, A. z. Yazaydin and J. T. Hupp, *J. Am. Chem. Soc.*, 2012, **134**, 15016–15021.
- H. W. Langmi, J. Ren, B. North, M. Mathe and D. Bessarabov, *Electrochim. Acta*, 2014, **128**, 368–392.
- Z. Hu, Y. Wang, B. B. Shah and D. Zhao, *Adv. Sustainable Syst.*, 2019, **3**, 1800080.
- P. Boyd, A. Chidambaram, E. García-Díez, C. Ireland, T. Daff, R. Bounds, A. Gładysiak, P. Schouwink, S. Moosavi, M. Maroto-Valer, J. Reimer, J. Navarro, T. Woo, S. Garcia, K. Stylianou and B. Smit, *Nature*, 2019, **576**, 253–256.
- R.-B. Lin, S. Xiang, H. Xing, W. Zhou and B. Chen, *Coord. Chem. Rev.*, 2019, 87–103.
- J. Gonzalez, K. Mukherjee and Y. J. Colón, *J. Chem. Eng. Data*, 2023, **68**, 291–302.
- S. Sircar, *Ind. Eng. Chem. Res.*, 2002, **41**, 1389–1392.
- A. Sturluson, M. T. Huynh, A. R. Kaija, C. Laird, S. Yoon, F. Hou, Z. Feng, C. E. Wilmer, Y. J. Colón, Y. G. Chung, D. W. Siderius and C. M. Simon, *Mol. Simul.*, 2019, **45**, 1082–1121.
- P. Z. Moghadam, A. Li, X.-W. Liu, R. Bueno-Perez, S.-D. Wang, S. B. Wiggin, P. A. Wood and D. Fairen-Jimenez, *Chem. Sci.*, 2020, **11**, 8373–8387.
- N. Rampal, A. Ajenifuja, A. Tao, C. Balzer, M. S. Cummings, A. Evans, R. Bueno-Perez, D. J. Law, L. W. Bolton, C. Petit, F. Siperstein, M. P. Attfield, M. Jobson, P. Z. Moghadam and D. Fairen-Jimenez, *Chem. Sci.*, 2021, **12**, 12068–12081.
- R. B. Getman, Y.-S. Bae, C. E. Wilmer and R. Q. Snurr, *Chem. Rev.*, 2012, **112**, 703–723.
- Q. Yang and C. Zhong, *J. Phys. Chem. B*, 2006, **110**, 17776–17783.
- P. Li, N. A. Vermeulen, C. D. Malliakas, D. A. Gómez-Gualdrón, A. J. Howarth, B. L. Mehdi, A. Dohnalkova, N. D. Browning, M. O'Keeffe and O. K. Farha, *Science*, 2017, **356**, 624–627.
- F.-X. Coudert and A. H. Fuchs, *Coord. Chem. Rev.*, 2016, **307**, 211–236.
- Y. G. Chung, J. Camp, M. Haranczyk, B. J. Sikora, W. Bury, V. Krungleviciute, T. Yildirim, O. K. Farha, D. S. Sholl and R. Q. Snurr, *Chem. Mater.*, 2014, **26**, 6185–6192.
- C. Wilmer, M. Leaf, C. Lee, O. Farha, B. Hauser, J. Hupp and R. Snurr, *Nat. Chem.*, 2012, **4**, 83–89.
- P. Wollmann, M. Leistner, U. Stoeck, R. Grünker, K. Gedrich, N. Klein, O. Throl, W. Grählert, I. Senkowska, F. Dreisbach and S. Kaskel, *Chem. Commun.*, 2011, **47**, 5151–5153.
- S. Li, Y. G. Chung and R. Q. Snurr, *Langmuir*, 2016, **32**, 10368–10376.
- M. H. Hiller, J. J. Lacatena and G. Q. Miller, *Hydrogen for hydroprocessing operations*, National Petroleum Refiners Association, Washington, DC, 1987.
- G. Sneddon, A. Greenaway and H. H. P. Yiu, *Adv. Energy Mater.*, 2014, **4**, 1301873.
- H. D. Frazier and A. L. Kohl, *Ind. Eng. Chem.*, 1950, **42**, 2288–2292.
- G. Maurin, P. L. Llewellyn and R. G. Bell, *J. Phys. Chem. B*, 2005, **109**, 16084–16091.
- R. Q. Snurr, A. T. Bell and D. N. Theodorou, *J. Phys. Chem.*, 1993, **97**, 13742–13752.
- G. B. Goh, N. O. Hodas and A. Vishnu, *J. Comput. Chem.*, 2017, **38**, 1291–1307.
- K. Mukherjee and Y. J. Colón, *Mol. Simul.*, 2021, **47**, 857–877.



- 27 Z. Shi, W. Yang, X. Deng, C. Cai, Y. Yan, H. Liang, Z. Liu and Z. Qiao, *Mol. Syst. Des. Eng.*, 2020, **5**, 725–742.
- 28 A. Erfani and M. Asghari, *J. Chem. Technol. Biotechnol.*, 2020, **95**, 2951–2963.
- 29 M. Z. Aghaji, M. Fernandez, P. G. Boyd, T. D. Daff and T. K. Woo, *Eur. J. Inorg. Chem.*, 2016, **2016**, 4505–4511.
- 30 Y. G. Chung, D. A. Gómez-Gualdrón, P. Li, K. T. Leperi, P. Deria, H. Zhang, N. A. Vermeulen, J. F. Stoddart, F. You, J. T. Hupp, O. K. Farha and R. Q. Snurr, *Sci. Adv.*, 2016, **2**, e1600909.
- 31 A. W. Thornton, C. M. Simon, J. Kim, O. Kwon, K. S. Deeg, K. Konstas, S. J. Pas, M. R. Hill, D. A. Winkler, M. Haranczyk and B. Smit, *Chem. Mater.*, 2017, **29**, 2844–2854.
- 32 N. S. Bobbitt and R. Q. Snurr, *Mol. Simul.*, 2019, **45**, 1069–1081.
- 33 M. Pardakhti, E. Moharreri, D. Wanik, S. L. Suib and R. Srivastava, *ACS Comb. Sci.*, 2017, **19**, 640–645.
- 34 G. S. Fanourgakis, K. Gkagkas, E. Tylianakis, E. Klontzas and G. Froudakis, *J. Phys. Chem. A*, 2019, **123**, 6080–6087.
- 35 C. M. Simon, R. Mercado, S. K. Schnell, B. Smit and M. Haranczyk, *Chem. Mater.*, 2015, **27**, 4459–4475.
- 36 M. Fernandez and A. S. Barnard, *ACS Comb. Sci.*, 2016, **18**, 243–252.
- 37 M. Fernandez, P. G. Boyd, T. D. Daff, M. Z. Aghaji and T. K. Woo, *J. Phys. Chem. Lett.*, 2014, **5**, 3056–3060.
- 38 B. J. Bucior, N. S. Bobbitt, T. Islamoglu, S. Goswami, A. Gopalan, T. Yildirim, O. K. Farha, N. Bagheri and R. Q. Snurr, *Mol. Syst. Des. Eng.*, 2019, **4**, 162–174.
- 39 A. Sturluson, M. T. Huynh, A. H. P. York and C. M. Simon, *ACS Cent. Sci.*, 2018, **4**, 1663–1676.
- 40 B. J. Befort, R. S. DeFever, G. M. Tow, A. W. Dowling and E. J. Maginn, *Machine Learning Directed Optimization of Classical Molecular Modeling Force Fields*, 2021.
- 41 R. Ma, Y. J. Colón and T. Luo, *ACS Appl. Mater. Interfaces*, 2020, **12**, 34041–34048.
- 42 G. M. Cooper and Y. J. Colón, *Mol. Syst. Des. Eng.*, 2023, **8**(8), 1049–1059.
- 43 F. Ricci, L. Rokach and B. Shapira, in *Recommender Systems Handbook*, 2010, vol. 1–35, pp. 1–35.
- 44 D. Cohn, Z. Ghahramani and M. Jordan, *Advances in Neural Information Processing Systems*, 1994.
- 45 B. Shahriari, K. Swersky, Z. Wang, R. P. Adams and N. de Freitas, *Proc. IEEE*, 2016, **104**, 148–175.
- 46 K. S. Walton and D. S. Sholl, *AIChE J.*, 2015, **61**, 2757–2762.
- 47 R. Krishna and J. M. van Baten, *ACS Omega*, 2021, **6**, 15499–15513.
- 48 G. Sivaraman, N. E. Jackson, B. Sanchez-Lengeling, Á. Vázquez-Mayagoitia, A. Aspuru-Guzik, V. Vishwanath and J. J. de Pablo, *Mach. Learn.: Sci. Technol.*, 2020, **1**, 025015.
- 49 V. Vovk, in *Kernel Ridge Regression*, ed. B. Schölkopf, Z. Luo and V. Vovk, Springer Berlin Heidelberg, Berlin, Heidelberg, 2013, pp. 105–116.
- 50 S. Suthaharan, in *Support Vector Machine*, Springer US, Boston, MA, 2016, pp. 207–235.
- 51 S. Myren and E. Lawrence, *Stat. Anal. Data Min.*, 2021, **14**, 606–623.
- 52 A. Kamath, R. A. Vargas-Hernández, R. V. Krems, T. Carrington and S. Manzhos, *J. Chem. Phys.*, 2018, **148**(24), 241702.
- 53 E. Uteva, R. S. Graham, R. D. Wilkinson and R. J. Wheatley, *J. Chem. Phys.*, 2018, **149**, 174114.
- 54 J. Vandermause, S. B. Torrisi, S. Batzner, Y. Xie, L. Sun, A. M. Kolpak and B. Kozinsky, *On-the-Fly Active Learning of Interpretable Bayesian Force Fields for Atomistic Rare Events*, 2019.
- 55 J. E. Santos, M. Mehana, H. Wu, M. Prodanović, Q. Kang, N. Lubbers, H. Viswanathan and M. J. Pycz, *J. Phys. Chem. C*, 2020, **124**, 22200–22211.
- 56 K. Mukherjee, A. W. Dowling and Y. J. Colón, *Mol. Syst. Des. Eng.*, 2022, **7**, 248–259.
- 57 E. Osaro, K. Mukherjee and Y. J. Colón, *Ind. Eng. Chem. Res.*, 2023, **62**(33), 13009–13024.
- 58 D. O. Abranches, E. J. Maginn and Y. J. Colón, *AIChE J.*, 2023, **69**(8), e18141.
- 59 C. E. Rasmussen and C. K. I. Williams, *Gaussian Processes for Machine Learning*, MIT Press, 2006.
- 60 A. L. Myers and J. M. Prausnitz, *AIChE J.*, 1965, **11**, 121–127.
- 61 D. Dubbeldam, S. Calero, D. E. Ellis and R. Q. Snurr, *Mol. Simul.*, 2016, **42**, 81–101.
- 62 A. K. Rappe, C. J. Casewit, K. S. Colwell, W. A. Goddard and W. M. Skiff, *J. Am. Chem. Soc.*, 1992, **114**, 10024–10035.
- 63 B. Eggimann, A. Sunnarborg, H. Stern, A. Bliss and J. Siepmann, *Mol. Simul.*, 2014, **40**, 101–105.
- 64 S. S.-Y. Chui, S. M.-F. Lo, J. P. H. Charmant, A. G. Orpen and I. D. Williams, *Science*, 1999, **283**, 1148–1150.
- 65 J. M. Castillo, T. J. H. Vlught and S. Calero, *J. Phys. Chem. C*, 2008, **112**, 15934–15939.
- 66 Q. Yang and C. Zhong, *J. Phys. Chem. B*, 2006, **110**, 17776–17783.
- 67 S. Wang, Q. Yang and C. Zhong, *Sep. Purif. Technol.*, 2008, **60**, 30–35.
- 68 C. M. Simon, B. Smit and M. Haranczyk, *Comput. Phys. Commun.*, 2016, **200**, 364–380.
- 69 D. Liu and J. Nocedal, *Math. Program.*, 1989, **45**, 503–528.
- 70 J. D. Novaković, A. Veljović, S. S. Ilić, Ž. Papić and M. Tomović, *Theory Appl. Math. Comput. Sci.*, 2017, **7**, 39.
- 71 S. J. Tan, L. Liu and J. W. Chew, *Langmuir*, 2021, **37**, 6754–6764.
- 72 L. Hamon, E. Jolimaître and G. D. Pirngruber, *Ind. Eng. Chem. Res.*, 2010, **49**, 7497–7503.
- 73 X. Cai, F. Gharagheizi, L. W. Bingel, D. Shade, K. S. Walton and D. S. Sholl, *Ind. Eng. Chem. Res.*, 2021, **60**, 639–651.
- 74 L. D. González and V. M. Zavala, *Comput. Chem. Eng.*, 2023, **170**, 108110.

